Meso-Cenozoic exhumation of the Beishan, southern Central Asian Orogenic Belt:

Insights from low-temperature thermochronology

Thesis submitted in accordance with the requirements of the University of Adelaide for an Honours Degree in Geology

Jack Alexander Gillespie

November 2014

THE UNIVERSITY of ADELAIDE

MESO-CENOZOIC EXHUMATION OF THE BEISHAN, SOUTHERN CENTRAL ASIAN OROGENIC BELT: INSIGHTS FROM LOW-TEMPERATURE THERMOCHRONOLOGY

RUNNING TITLE

Meso-Cenozoic evolution of the Beishan

ABSTRACT

The Beishan Orogenic Collage (BOC) is located in the south of the Central Asian Orogenic Belt (CAOB) and formed during the final consumption of the Paleoasian Ocean in the Late-Permian to Middle-Triassic. This study applies low temperature thermochronology to constrain the Meso-Cenozoic exhumation history of the BOC. Apatite fission track and U-Th-Sm/He data obtained for granitoid samples along a north-south transect through the BOC suggest evidence for three distinct phases of exhumation during (1) the Late Triassic - Early Jurassic (~225 – 180 Ma), (2) Early - mid Cretaceous (~130 – 95 Ma) and (3) Late Cretaceous - Early Palaeogene (~75 – 60 Ma). Samples from northern Beishan reveal a more profound early to middle Cretaceous signal and a weaker Late Triassic - Early Jurassic signal than those in southern Beishan. A potential explanation for this discrepancy is the presence of the Xingxingxia fault in the northern BOC which is interpreted to have undergone repeated reactivation throughout the Mesozoic, exposing deeper exhumed sections of the BOC. The fault may thus have acted as a control on exhumation in the region. This pattern is consistent with results from elsewhere in the CAOB such as in the Tianshan and the Altai, where regional widespread exhumation occurred since the Early Cretaceous while major fault zones record localised exhumation during the Late Cretaceous – Early Palaeogene. Additional late Cretaceous – early Palaeogene cooling ages found only in the south of the BOC suggest that exhumation at that time was more localised and didn't reach the northern margins of the study area.
Our results indicate that the Triassic - early Jurassic and early to middle Cretaceous exhumation events in Central Asia were more widespread than previously anticipated, extending to the northern margin of the Tarim Craton. This observation hence refines the existing tectonic history models for Central Asia.

KEYWORDS

Mesozoic, Cenozoic, exhumation, thermochronology, Beishan, CAOB, intracontinental, AFT.

TABLE OF CONTENTS

LIST OF FIGURES AND TABLES

INTRODUCTION

The Beishan Orogenic Collage (BOC) of NW China is composed of several Neoproterozoic to Palaeozoic arcs and ophiolitic melanges, which were accreted and amalgamated during the Ordovician to middle Triassic (Xiao *et al.,* 2010). The BOC is located in the south of the Central Asian Orogenic Belt (CAOB) and is flanked by the terminal sutures of the CAOB, the Tianshan and Solonker sutures, which record the progressive closure and final consumption of the Paleoasian Ocean in the Late Permian to the Middle Triassic (Xiao *et al.,* 2009a). While the amalgamation history of the CAOB ceased during the Late Permian – Middle Triassic, its tectonic history was far from complete (e.g. De Grave *et al.,* 2007).

Significant intracontinental deformation post-dating the amalgamation of the CAOB is evident today in the series of large mountain ranges in Central Asia (e.g. the Tianshan and the Altai with peaks up to 7,400m). Through the application of low- temperature thermochronology such as the apatite fission track (AFT) method, previous studies have uncovered largely consistent results in the Tianshan, the Altai and in northern Tibet, which suggest several distinct periods of basement cooling related to exhumation (Dumitru *et al.,* 2001, Jolivet *et al.,* 2001, Glorie *et al.,* 2010, Jolivet *et al.,* 2010, Glorie *et al.,* 2011, De Grave *et al.,* 2012, Glorie *et al.,* 2012, De Grave *et al.,* 2013, Macaulay *et al.,* 2014). Intracontinental deformation in Central Asia has generally been attributed to three main tectonic events that occurred at the margins of the Meso-Cenozoic Eurasian continent and that induced episodes of intraplate reactivations within the CAOB. These events are (1) the Mesozoic to Early Cenozoic Cimmerian collisions at the Mesozoic southern Eurasian margin, (2) the Mesozoic Mongol-Okhotsk orogeny at

the eastern Mesozoic Eurasian margin and (3) the Cenozoic India-Eurasia collision (e.g. Bullen *et al.*, 2001, Dumitru *et al.*, 2001, Jolivet *et al.*, 2001, De Grave *et al.*, 2012, Glorie *et al.*, 2012). Although Mesozoic exhumation mostly seems to have occurred on a regional scale, Late Cretaceous and Cenozoic uplift within the CAOB is thought to be strongly controlled by the inherited basement architecture of the CAOB. Within this framework, ancient ophiolitic sutures and other major fault zones are thought to have undergone and recorded repeated reactivations and are thus prime localities to study the exhumation history of the CAOB (Jolivet *et al.*, 2010, Glorie *et al.*, 2011, Glorie *et al.*, 2012, De Grave *et al.*, 2013).

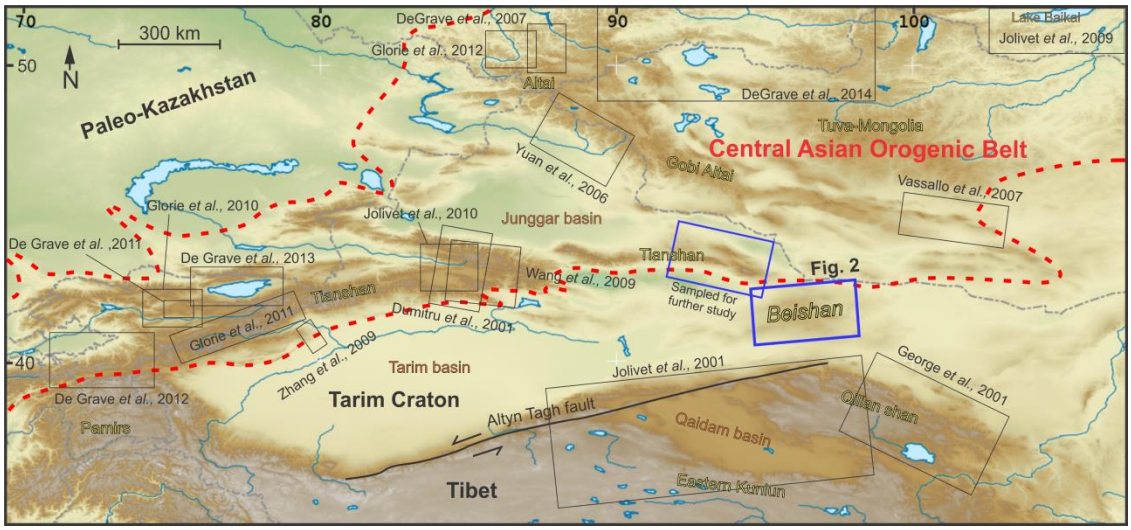

Figure 1: Map of the Central Asian Orogenic Belt with indication of the Beishan study area (blue) and showing the location of other low-T thermochronological studies in the region (black).

In contrast to the neighbouring Tianshan, the low-temperature exhumation history of the Beishan has not yet been studied and is hence very poorly understood (Fig. 1). This is significant, as the Beishan occupies a critical position in the southern CAOB, and although its relief is less profound than the bordering Tianshan and Tibetan mountain ranges, the region is characterised by significant topography as well (~2500m max elevation). It is currently unclear whether the modern relief of the Beishan represents

relict topography from the final Triassic amalgamation of the CAOB or the product of younger deformation, such as we see in the neighbouring Tianshan.

The purpose of this study is therefore to constrain the low-temperature cooling history of the Beishan in order to improve our understanding of the thermo-tectonic history of the southern CAOB. We use the results of AFT analysis (using the LA-ICP-MS method described in Hasebe *et al.,* (2004)) in combination with apatite (U-Th-Sm)/He (AHe) analysis to model the thermal history of the BOC between 120^{0}C and 45^{0}C. This approach enables the identification of distinct exhumation episodes that can be linked with the far-field collisions and orogenesis at the Eurasian margins and provides insight on the propagation of stress from the margins to the continental interior (e.g. De Grave *et al.,* 2007, Glorie *et al.,* 2011).

GEOLOGICAL SETTING

The Beishan is one of the southernmost units of the Central Asian Orogenic Belt (CAOB), a huge and long-lived accretionary system that was active from around 1000 Ma to 250 Ma (e.g. Sengor *et al.,* 1993, Khain *et al.,* 2002, Xiao *et al.,* 2009b). Accretionary orogenesis throughout the CAOB was terminated with the northwards movement of the Tarim and North China cratons and the final closure of the Paleoasian Ocean during the Late-Permian to middle Triassic (Xiao *et al.,* 2003, Zhang *et al.,* 2007, Xiao *et al.,* 2009b). The terminal sutures of the CAOB flank the Beishan and although it has not been proven, it seems likely that these sutures are connected (Xiao *et al.,* 2010). Prior to the middle Triassic, the region remained directly subjected to plate boundary stresses as amalgamation of the CAOB was not yet complete (Zhang *et al.,* 2007, Xiao *et al.,* 2009a, Xiao *et al.,* 2010). Further details on the pre middle Triassic tectonic history are beyond the scope of this paper and will not be discussed in any further depth.

For comprehensive discussions concerning the accretion of the CAOB see Windley *et al.,* (2007) and Xiao *et al.,* (2010).

Several studies have used $^{40}Ar/^{39}Ar$ thermochronology to explore intracontinental deformation in or near the Beishan; however they have focussed primarily on deciphering the timing of ductile to early brittle deformation along important bounding structures. The Altyn Tagh fault zone lies on the northern margin of the Tibetan Plateau and is directly to the south of the Beishan (Fig. 1). It has undergone several phases of sinistral ductile deformation since the Paleozoic, and shares many elements of its cooling history with the eastern Kunlun to the south and northern Qaidam to the east (Fig. 1; e.g. Liu *et al.,* 2005, Wang *et al.,* 2005). $^{40}Ar/^{39}Ar$ dating of muscovite (Mu), biotite (Bt) and K-feldpsar (Kfs) in the Altyn Tagh, eastern Kunlun and north-eastern Qaidam basin all yielded cooling events at 250-230 Ma, 160-150 Ma and at 120-90 Ma (Wang et al., 2005). Most authors cite the Qiangtang collision as the driving force behind the Triassic exhumation (e.g. Jolivet *et al.,* 2010, De Grave *et al.,* 2011), while Wang et al., (2005) proposes a diachronous model for the collision of the Lhasa block in order to explain the two Jurassic-Cretaceous events.

The Xingxingxia shear zone at the northern margin of the BOC is the focus of the only currently published thermochronological study in the Beishan region. This ENE trending shear zone was active around 240-235 Ma (based on $^{40}Ar/^{39}Ar$ Mu, Bt, Kfs), with sinistral shear sense and similar stretching lineation orientations as found for the Altyn Tagh fault zone (Wang et al., 2010). Based on this evidence Wang *et al.,* (2010) considered the Xingxingxia fault to be a northern branch of the Altyn Tagh fault that experienced ductile deformation during initial Triassic fault activity, similar to the

Altyn Tagh fault. Later brittle reactivations during later Mesozoic and Cenozoic events have not been reported for the Xingxingxia fault zone.

METHODS

Apatite fission track and (U-Th-Sm)/He method

The apatite fission track (AFT) method relies on the temperature dependant annealing of natural fission tracks in apatite crystals and is used to reconstruct the thermal history of a targeted study area between 120^{0}C and 60^{0}C. Fission tracks are created when the fission particles of a decayed ^{238}U atom blast a ~16.3μm linear track through the structure of an apatite crystal (Gleadow *et al.,* 1986b).

These fission tracks anneal instantaneously (on a million year time-scale) above ~120^{0}C and are preserved fully below ~60^{0}C. The range from 120-60^{0}C is known as the partial annealing zone, in which fission tracks shorten and are thus only partially retained (Wagner *et al.,* 1989). Using the fission track density and uranium concentration in the apatite grains, the fission track age can be determined, which reflects the timing of the grains passage though the apatite partial annealing zone (APAZ). Measurements of fission track lengths provide additional information about the rate of cooling through the APAZ, with an increasing proportion of short fission tracks indicating slower cooling through the APAZ (Gleadow *et al.,* 1986a).

The apatite chemistry also influences the annealing rate of fission tracks and can be measured using an electron micro-probe analyser. The Cl/F ratio of an apatite crystal has a strong control on the annealing rate of fission tracks, and variation in this ratio between grains in a single sample may indicate different preservation potentials of low-temperature cooling events (Green *et al.,* 1986). This process makes it possible to derive

multiple cooling events within a single sample as apatite grains that anneal more slowly may preserve older thermal events while those that anneal more rapidly may have been reset by younger shallow crust thermal events.

The apatite (U-Th-Sm)/He (AHe) method is comparable to the AFT method, but is sensitive to lower temperature (40-80^{0}C) (Ehlers and Farley 2003, Evans *et al.,* 2005). Helium atoms (α particles) are decay products of U, Th and Sm which accumulate proportionally over time in the apatite crystals. As the helium atoms are in the gas phase, they will escape from the crystals at high temperatures (>75^{0}C) but will be partially retained when the sample cools between 75-45^{0}C. Measuring the concentration of He with respect to U, Th and Sm makes it possible to determine a U-Th-Sm/He age which aids in the refinement of the thermal history of the study region.

Laboratory Processing

Samples were crushed and sieved using standard procedures and the apatite fraction was separated by the conventional magnetic and heavy liquid method at the Institute of Geology and Geophysics, Chinese Academy of Sciences (IGGCAS). Fifteen samples were analysed with the AFT method, using the Laser Ablation Inductively Coupled Plasma Mass Spectrometry (LA-ICP-MS) technique described in Hasebe *et al.,* (2004), as opposed to the conventional AFT technique. Three of these samples were selected for analysis with the AHe method.

APATITE FISSION TRACK ANALYSIS

Apatite grains were picked and mounted in epoxy resin and sample mounts were ground and polished to expose internal sections. They were then chemically etched in a 5M HNO_3 solution for 20 seconds at 20^{0}C to reveal the natural fission tracks. The fission

track density within individual apatite grains, which is a measure of the cooling age through the fission track closure temperatures (60-120^{0}C), was determined by counting the number of tracks in a reference grid. Where possible, at least 1000 tracks distributed between minimum 20 grains were counted per sample. Horizontal confined tracks, a measure of the cooling rate through the AFT closure temperatures, were measured under a high-powered (1000X magnification) microscope. One hundred confined tracks per sample were also measured if sample quality allowed. The uranium concentration of each counted grain was then determined through spot analyses on an Agilent 7700s mass spectrometer, coupled with a Resonetics M-50 laser system (Table 2). Calibrations were carried out using NIST 610, 612, 614 and Durango apatite standards. Measurement of the Cl/F ratio in individual grains was performed on the JEOL JXA 8100 electron probe microanalyser (EPMA) at IGGCAS.

Table 1: Analytical details for the LA-ICP-MS as used for AFT dating

ICPM-MS	
Brand and model	Agilent 7700s
Forward power	1300 W
Gas flows (L/min)	
Cool (Ar)	15.00
Auxiliary (Ar)	0.89
Carrier (He)	0.70
Sample (Ar)	0.93
Laser	
Type of Laser	Excimer laser
Brand and Model	Resonetics M-50-LR
Laser wavelength	193nm
Pulse duration	20 ns
Spot size	32 µm
Repetition rate	5 Hz
Energy attenuation	50%
Laser fluency	~7 J/cm^{-2}
Laser warm up (background collection)	15 s
Data acquisition parameters	
Data acquisition protocol	Time-resolved analysis
Scanned masses	235, 238, 43
Samples per peak	1
Number of scans per peak	1
Detector mode	Pulse counting
Detector deadtime	35 ns
Background collection	15 s
Ablation for age calculation	30 s
Washout	15 s
Standardisation and data reduction	
Primary standard used	NIST 610, NIST 612, NIST 614 calibration line
Secondary standard used	Durango apatite (McDowell et al. 2005)*
Data reduction software used	In-house Excel® spreadsheet

*McDowell, F.W., McIntosh, W.C., Farley, K.A., 2005. A precise 40Ar–39Ar reference age for the Durango apatite (U–Th)/He and fission-track dating standard. Chemical Geology 214, 249-263.

APATITE (U-TH-SM)/HE ANALYSIS

Apatite (U-Th-Sm)/He analysis was performed on three samples. Approximately 10-15 high quality euhedral, inclusion-free, unbroken apatite crystals with grain sizes larger

than 70µm per sample were selected. These grains were sent to the John De Laeter Centre at Curtin University for analysis. These results were used to further refine the AFT thermal history models in the ~40-80^{0}C temperature range. Due to the overlapping thermal sensitivity range of the AFT (60-120^{0}C) and AHe methods, fast cooling is often reflected in identical ages being produced by the two methods. Multiple methods indicating a large cooling event implies that an important phase of exhumation occurred at that time.

MODELLING

Individual AFT ages and Cl/F data for individuals grains were loaded into the Radial Plotter software (Vermeesch 2009) which uses a radial plot to calculate the central age of the single grain ages for each sample. This central age is reported in the data table in the results section and gives the best estimation for the apparent AFT cooling age of the analysed sample. However, multiple AFT age-populations may be present in samples with large (>20%) age dispersion and the radial plot is further used as a tool to identify them. The automatic mixture model was used in RadialPlotter to decompose the dataset into statistically acceptable age-components

The age-peak discrimination process was aided and visually validated using the analysed chemical Cl/F ratios of each grain. As discussed above, different Cl/F ratios reflect different annealing kinetics of the fission tracks and thus enable detection of multiple cooling events in one sample.

HeFTy modelling software (Ketcham 2005) was used to model the cooling path (t-T evolution) based on the apparent apatite fission track ages and the confined length data.

High and low temperature constraints were added to the modelling space to allow the model to run. Other geological constraints (e.g. ^{40}Ar-^{39}Ar cooling ages) were inserted if available and possible cooling paths through these constraints were simulated using a Monte-Carlo approach. If a generated cooling path matched the inserted AFT data with a goodness of fit > 0.05, the path was retained as a green 'statistically acceptable' path. If the cooling path matched the inserted AFT data with a goodness of fit > 0. 5, it was retained as a purple 'good fit' path. After the modelling was terminated based on a user-determined threshold (typically when >100 good paths were obtained), good fit-envelopes were displayed which visualise the thermal history of the investigated sample between ~120^{0}C and ambient temperatures.

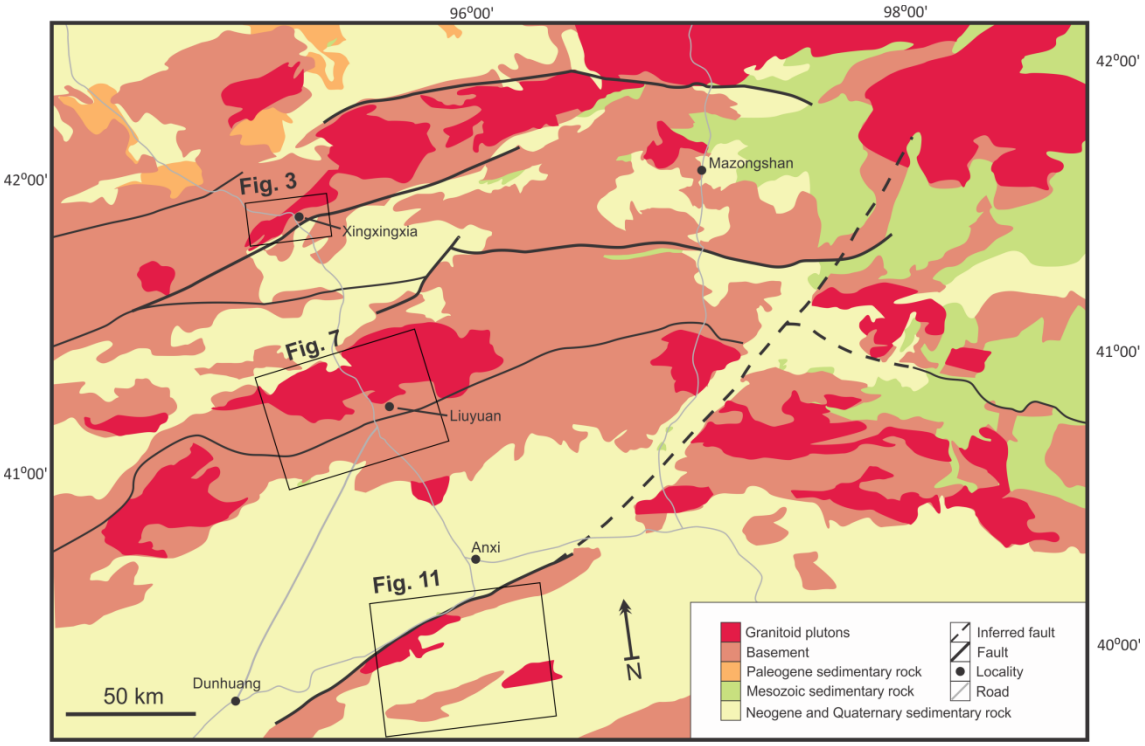

Figure 2: Simplified map of the Beishan area showing the distribution of sedimentary and basement rocks. Figures 3, 7 and 11 are marked. Modified after Xiao *et al.* (2010), CTAJ (2007)

Table 2: Sample location and lithology details.

Sample	Latitude	Longitude	Altitude (m)	Locality	Lithology
BH01	N41°47.281	E95°07.890	1803	Xingxingxia	Granite/mylonite
BH02	N41°06.492	E95°30.911	1809	Liuyuan	Diorite/pink granite
BH03	N40°59.291	E95°02.335	1737	Liuyuan	Granodiorite
BH04	N40°59.160	E95°02.325	1740	Liuyuan	Augen gneiss
BH05	N40°07.112	E95°43.288	1498	Dunhuang	Granodiorite vein
BH06	N40°07.079	E95°43.311	1538	Dunhuang	Pinkish granite vein
BH07	N40°06.372	E95°51.897	1616	Dunhuang	Granulite
BH08	N41°06.187	E95°24.702	1799	Liuyuan	Granite - granodiorite
BH09	N41°04.127	E95°16.352	1802	Liuyuan	Coarse diorite
BH10	N41°16.907	E95°21.562	1822	Liuyuan	Coarse Bt-Kspr granite
BH12	N41°47.758	E95°08.343	1808	Xingxingxia	Granite
BH13	N41°48.458	E95°08.856	1832	Xingxingxia	Granite
BH14	N41°48.806	E95°07.091	1833	Xingxingxia	Granite
BH15	N41°49.014	E94°58.010	1590	Xingxingxia	Diorite
BH16	N41°49.014	E94°58.010	1590	Xingxingxia	Granodiorite

RESULTS

Sample Location

In order to explore the thermal history of the BOC, 16 samples were collected along a 220km long roughly N-S transect, perpendicular to the general strike of the major structural contacts and suture zones in the region (Fig. 2). Fifteen samples were analysed using the apatite fission track method (one sample was discarded due to poor apatite quality). Three general sampling regions within the BOC area can be defined (Fig. 2): the Xingxingxia fault zone (Fig. 3), the vicinity of Liuyuan town (Fig. 7), and near Dunhuang (Fig. 11). One sample from each of these regions was additionally analysed using the AHe method. Major structural features were targeted during sampling in order to evaluate the effect of these structures on the timing and rate of uplift and exhumation. Sample locations and rock descriptions are detailed in Table 1 and sample localities are shown in Fig. 2. The samples were taken from Paleozoic crystalline rocks with granitic to dioritic composition, in some cases exhibiting gneissic or granulite facies metamorphism.

The Xingxingxia fault zone is a prominent feature in the north of the sampling area, from which six AFT samples (BH01, BH12, BH13, BH14, BH15 and BH16) were analysed. Further to the south, six AFT samples (BH02, BH03, BH04, BH08, BH09 and BH10) were taken in the vicinity of Liuyuan town. The three southernmost AFT samples (BH05, BH06 and BH07) were taken near Dunhuang. BH12 from Xingxingxia, BH09 from Liuyuan and BH07 from Dunhuang were chosen for AHe analysis based on their apatite and AFT data quality.

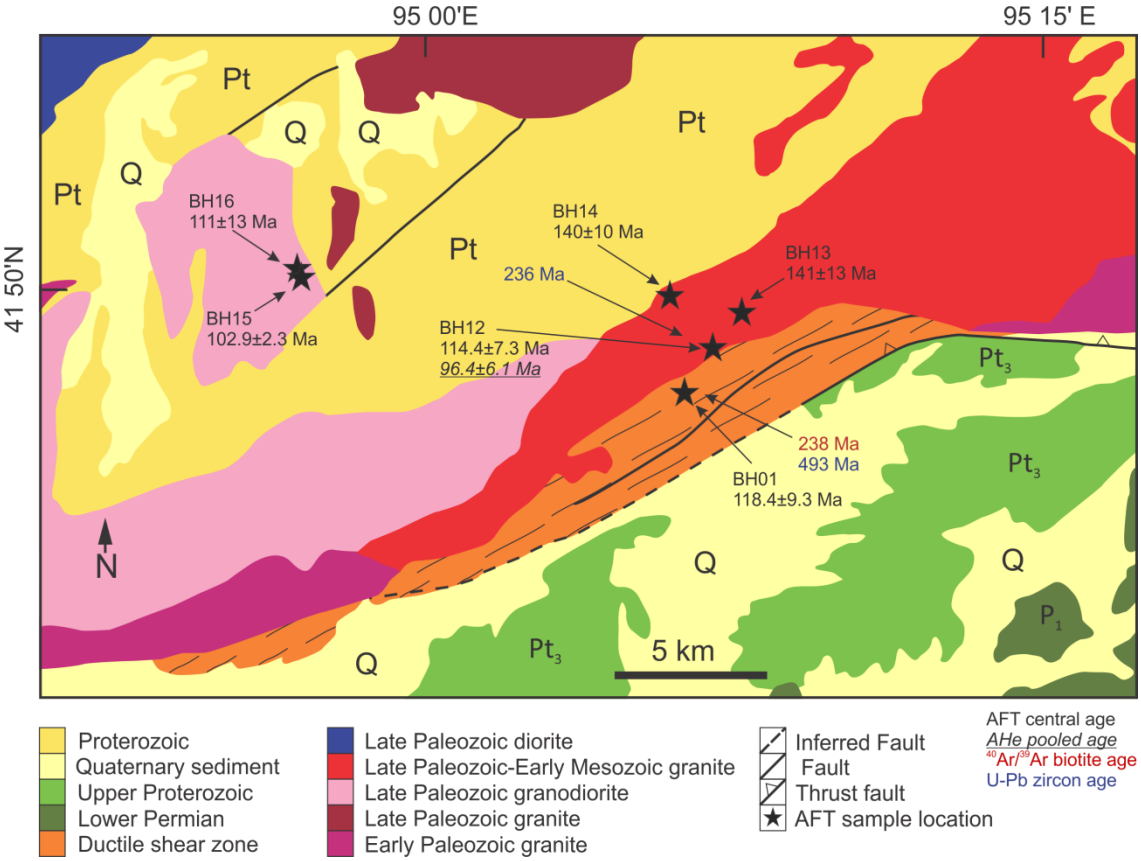

Figure 3: Map of the Xingxingxia fault zone and surroundings. AFT central ages and pooled AHe ages are from this study and are shown by star symbols. $^{40}Ar/^{39}Ar$ biotite and U-Pb zircon ages are from Wang et al. 2010. Modified after Wang et al. 2010

Xingxingxia fault zone

The Xingxingxia samples (Fig. 3) yield central AFT ages ranging from 102.9±2.3 Ma to 140±10 Ma (Fig. 4). BH01 and BH12 were sampled closest to the Xingxingxia fault and

have central ages of 118.4±9.3 Ma and 114.4±7.8 Ma respectively. Age-peak discrimination using RadialPlotter returned significant age populations at around 100 Ma in both samples, as well as a significantly older population, however the older age-component is not well constrained (Fig. 4). BH13 and BH14 are further north of the fault and have central ages of 141±13 Ma and 140±10 Ma. Both samples yield better defined age-peaks of ~200-250 Ma and ~115-140 Ma. Sample BH13 additionally yields two younger grains of ~70 Ma (Fig. 4). BH15 and BH16 yield central ages of 102.9±2.3 Ma and 111±13 Ma with little age dispersion, which could not be further discriminated into multiple age-components in RadialPlotter. Within each of the six samples there is little correlation between the AFT age components and the Cl/F ratios (Fig. 4).

Table 3: AFT dating results. ρ_s is the density of spontaneous tracks (in 10^5 tracks/cm^2). N_s is the number of counted spontaneous tracks. *n* is the number of counted grains. ^{238}U is in pmm. CaO is in wt%. The AFT age (t) is given in Ma and was calculated using the Hasebe *et al.*, (2004) equation.

Sample	ρ_s	N_s	*n*	^{238}U	1σ	CaO	t (Ma)	1 σ
BH01	8.38	692	14	16.01	0.13	54.70	118.4	9.3
BH02	10.94	429	17	20.72	0.18	54.47	132	11
BH03	15.22	644	14	35.94	0.31	54.56	109.3	4.3
BH04	5.56	503	19	12.14	0.12	54.57	125	10
BH05	9.91	337	9	12.34	0.13	55.16	156	11
BH06	11.06	603	19	20.95	0.18	54.72	141.4	9.9
BH07	13.45	1341	15	18.71	0.13	55.24	167.5	9.8
BH08	12.56	947	15	28.014	0.23	54.91	108.1	8
BH09	10.07	921	19	16.66	0.13	54.79	139.8	8.7
BH10	6.98	199	11	11.18	0.12	54.78	150	13
BH12	8.43	929	20	17.51	0.31	54.23	114.4	7.3
BH13	13.74	805	15	23.56	0.17	54.70	141	13
BH14	11.91	754	19	22.69	0.17	54.40	140	10
BH15	42.41	2010	15	95.85	0.61	54.99	102.9	2.3
BH16	19.55	258	6	39.28	0.79	54.42	111	13

In order to evaluate the thermal history of the Xingxingxia fault zone on a broader scale, a pooled radial plot was constructed using all the AFT data from the region. In this plot, the AFT age peaks are compared with additional AHe results in order to more

accurately constrain the cooling pulses recorded in the Xingxingxia fault zone. The pooled Xingxingxia radial plot (Fig. 5) yields a central age of 121.3±4.0 Ma, which can be decomposed into three age-peaks at 99.5±2.6 Ma, 130.8±5.1 Ma and 226±13 Ma. Apatites with higher Cl/F ratios almost exclusively exhibit younger AFT ages (~100 Ma age peak; Fig. 5). The correlation between Cl/F ratio and the age of grains in this case suggests that the peaks are preserving different cooling events depending on the annealing kinetics of the apatite crystals, which verifies the age-peak discrimination process.

The length distributions for these samples yield mean lengths of 12.16µm – 13.23µm, with standard deviations of 1.01µm – 1.12µm (Fig. 4), which are indicative of moderate-fast cooling rates. An additional AHe analysis of BH12 produced age components of 124.4±7.9 Ma and 96.4±6.1 Ma (Table 4). The two AHe age components clearly mimic the two youngest AFT age components, which are indicative of fast cooling at ~130-125 Ma and ~100-95 Ma (Fig 5).

Table 4: AHe dating results. Concentrations for U, Th and Sm are given in ppm. ^{4}He concentration is in nmol/µg. Ft is the α-ejection correction factor. Number of aliquots for each age given in brackets. Single aliquot ages in italics. AFT central ages listed for comparison.

Sample	U	Th	Sm	Th/U	He	Ft	t (AHe)	t (AFT)
BH07	27.95	9.18	22.63	0.35	0.59	0.77	*(1) 126.8±8.4* (2) 60.6±4.2	167.5±9.8
BH09	59.97	110.16	12.52	1.76	1.74	0.72	(4) 101.5±6.5 *(1) 70*.3±4.5	139.8±8.7
BH12	52.01	94.66	49.92	2.2	1.6	0.73	*(1) 124.4±7.9* (2) 96.4±6.1	114.4±7.3

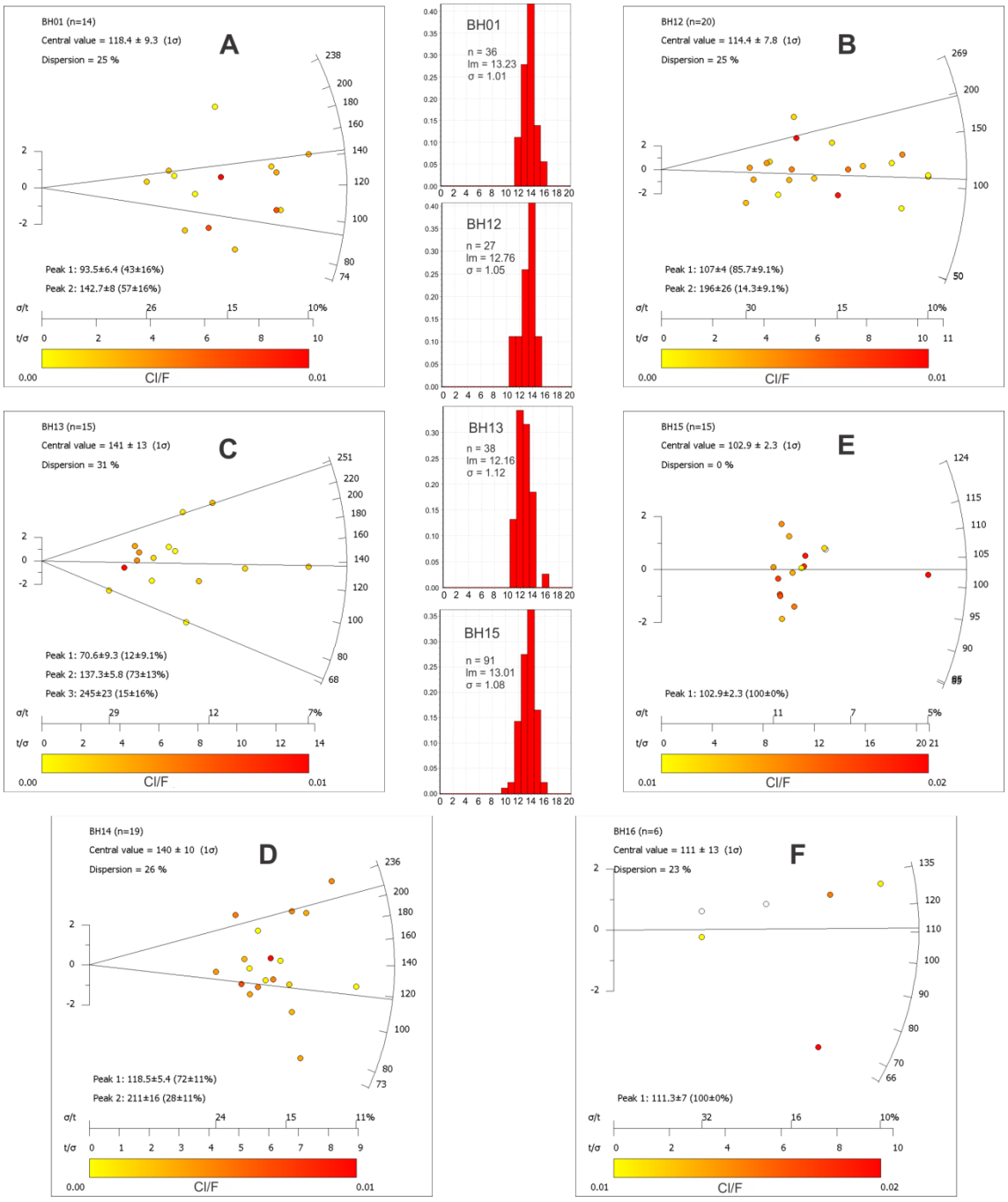

Figure 4: Radial plots of calculated AFT cooling ages for each sample location within the Xingxingxia fault zone (A-F). Central values were calculated and where the data shows a high degree of age dispersion (>20%), age-peak discrimination was performed using the automatic mixture model of the RadialPlotter software (Vermeesch 2009). The percentage of the data contained in each peak as well as age dispersion within each peak is shown in brackets with the age of each peak. The Cl/F ratio is indicated by a red/yellow colour scale. The X-axis shows decreasing uncertainty from left to right. The curved Y-axis on the right of the plot shows increasing age in Ma and the Y-axis to the left of the plot displays standard deviations from the central age. Frequency plots depict length distribution of apatite fission tracks in samples from the area. n is the number of measured confined tracks, l_m is the average track length and σ is the standard deviation of the track lengths distribution.

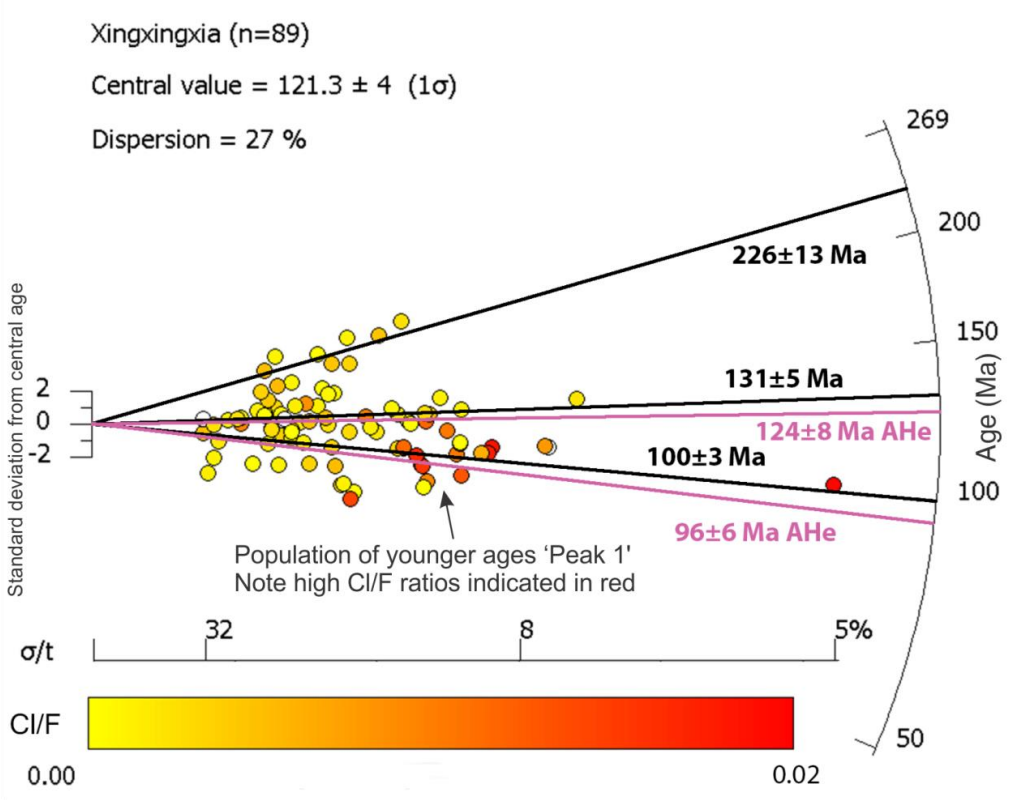

Figure 5: Radial plots of calculated AFT cooling ages combining all samples from the Xingxingxia fault zone. The data show a high degree of dispersion (~27%) and therefore age-peak discrimination was performed using the automatic mixture model of the RadialPlotter software (Vermeesch 2009). Resultant age-peaks are shown in black. AHe ages are shown in pink and clearly mimic the youngest two AFT age-peaks. The Cl/F ratio is indicated by a red/yellow colour scale. As shown, apatites with the highest Cl/F ratios (red symbols) record the youngest AFT age peak of ~100 Ma.

Thermal history modelling was performed in order to evaluate the cooling history of the Xingxingxia fault zone. The thermal history model for BH01 uses $^{40}Ar/^{39}Ar$ biotite (~240 Ma), and potassium feldspar (~215 Ma) cooling ages from Wang *et al.*, (2010) in addition to the AFT central age (118.4±9.3 Ma) from this study. The thermal history model shows rapid cooling through the APAZ during the Triassic – Early Jurassic (~250-180 Ma) followed by slow cooling during the middle Jurassic and early Cretaceous (~180-130 Ma) and increased cooling during the early – middle Cretaceous (~130-110 Ma). From ~110 Ma onwards, the thermal history model shows very slow cooling from ~50^{0}C until present-day outcrop temperatures (Fig. 6). While the remainder of the samples do not have the advantage of other published data to assist in

the modelling of their thermal histories, additional AHe data for BH12 made it possible to refine the thermal history model for this sample. BH12 and BH15 show a similar cooling history to that of BH01, although they are less constrained at higher temperatures. Slow cooling prior to 130 Ma is interrupted by a rapid phase of cooling through the APAZ from ~130-110 Ma. Slow cooling resumes after 110 Ma and continues to the present.

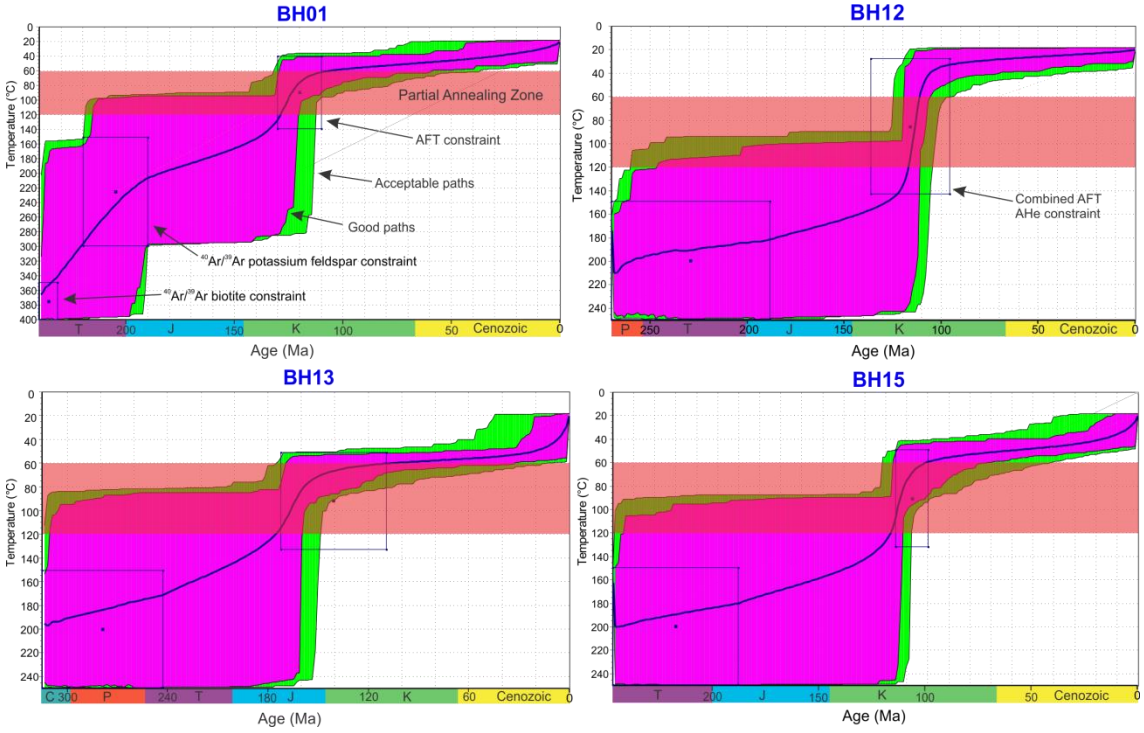

Figure 6: Thermal history models for samples in the vicinity of Xingxingxia generated using HeFTy software (Ketcham 2005). Modelling strategy uses box-constraints for AFT ages (this study) and any other published data to generate paths of varying probability for the thermal history. The purple envelope encompasses 'Good' (>0.5) probability pathways and the green envelope 'Acceptable' (>0.05) pathways. The blue line represents the weighted mean path of the model. The Partial Annealing Zone (PAZ) is highlighted in red. $^{40}Ar/^{39}Ar$ ages (Bt-245±5 Ma, Kfs-210±20 Ma) for BH01 from Wang et al. 2010.

Sample BH13, which was sampled further north from the Xingxingxia fault, underwent only moderate cooling and passed through the APAZ slightly earlier at 170-140 Ma. Its post-Jurassic thermal history shows thermal quiescence until the late Cenozoic where an apparent increase in the cooling rate brought the sample to the surface. Note that this final increase in cooling during the Late Cenozoic is exhibited by all models, but is

more profound for sample BH13. The relevance of this final cooling step is disputable and may be a modelling artefact (e.g. Ketcham *et al.*, 1999).

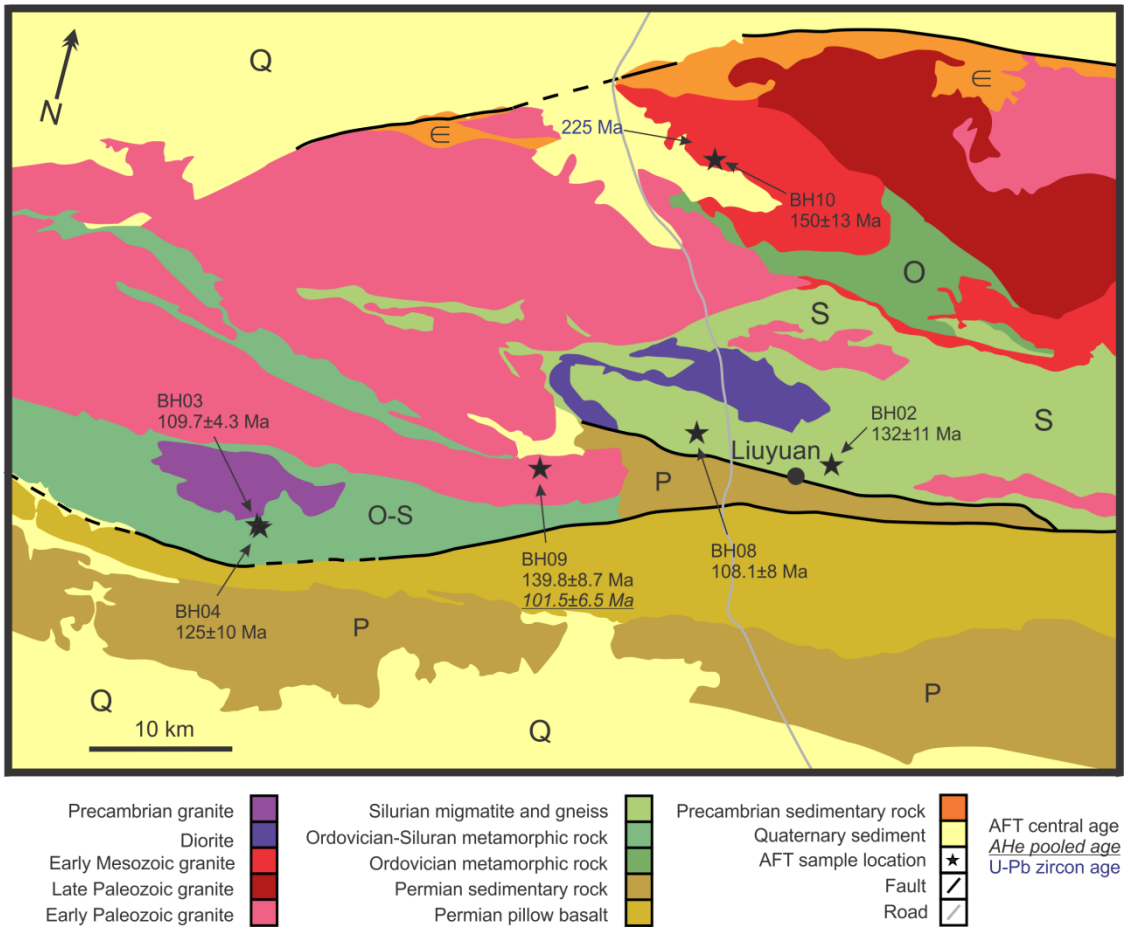

Figure 7: Map of Liuyuan town and surroundings. AFT central ages and pooled AHe ages are from this study and are shown by star symbols. U-Pb zircon ages from Li et al. 2012.Modified after Xiao et al. 2010, Li et al. 2012, The Second Geological Team of the Gansu Bureau of Geology and Mineral Deposits 1967.

Liuyuan study area

The Liuyuan samples yield central ages ranging from 108.1±8.0 Ma to 150±13 Ma (Fig. 7,8). Sample BH02 was taken immediately to the NE of Liuyuan town and yields a central age of 132±11 Ma. Samples BH03 and BH04 were collected approximately 40km WSW of Liuyuan town and yield central ages of 109.7±4.3 Ma and 125±10 Ma. BH04 contained enough dispersion to allow discrimination into two age-peaks at 171±15 Ma and 100.1±7.6 Ma while BH03 could not be further broken down. BH08

and BH09 were sampled 10-20km WSW of Liuyuan town and yield central ages of 108.1±8.0 Ma and 139.8±8.7 Ma. Age-peak discrimination yields populations at 176±14 Ma and 97.2±3.6 Ma for BH08 and 210±16 Ma and 125.2±5.8 Ma for BH09. Sample BH10 ~20km to the NW of Liuyuan town yields a central age of 150±10 Ma. Within each of the six samples there is no apparent correlation between the individual AFT age and the Cl/F ratios of the grains.

The combined Liuyuan plot (Fig. 9) yields a central age of 125±4 Ma and age-peaks at 185±7 Ma and 108±3 Ma, again with no obvious correlation between the AFT age-peaks and Cl/F ratios. The length distributions for these samples have mean lengths of 12.79µm – 13.79µm, with standard deviations of 0.91µm – 1.31µm indicating fast cooling rates. Sample BH09 was chosen for AHe analysis, yielding AHe age-populations of 101.5±6.5 Ma and 70.3±4.5 Ma. The older AHe age mimics the younger Liuyuan AFT age-peak, indicating rapid cooling at 110-95 Ma. The youngest AHe age corresponds to the youngest individual AFT ages and may indicate a third cooling event at ~70 Ma.

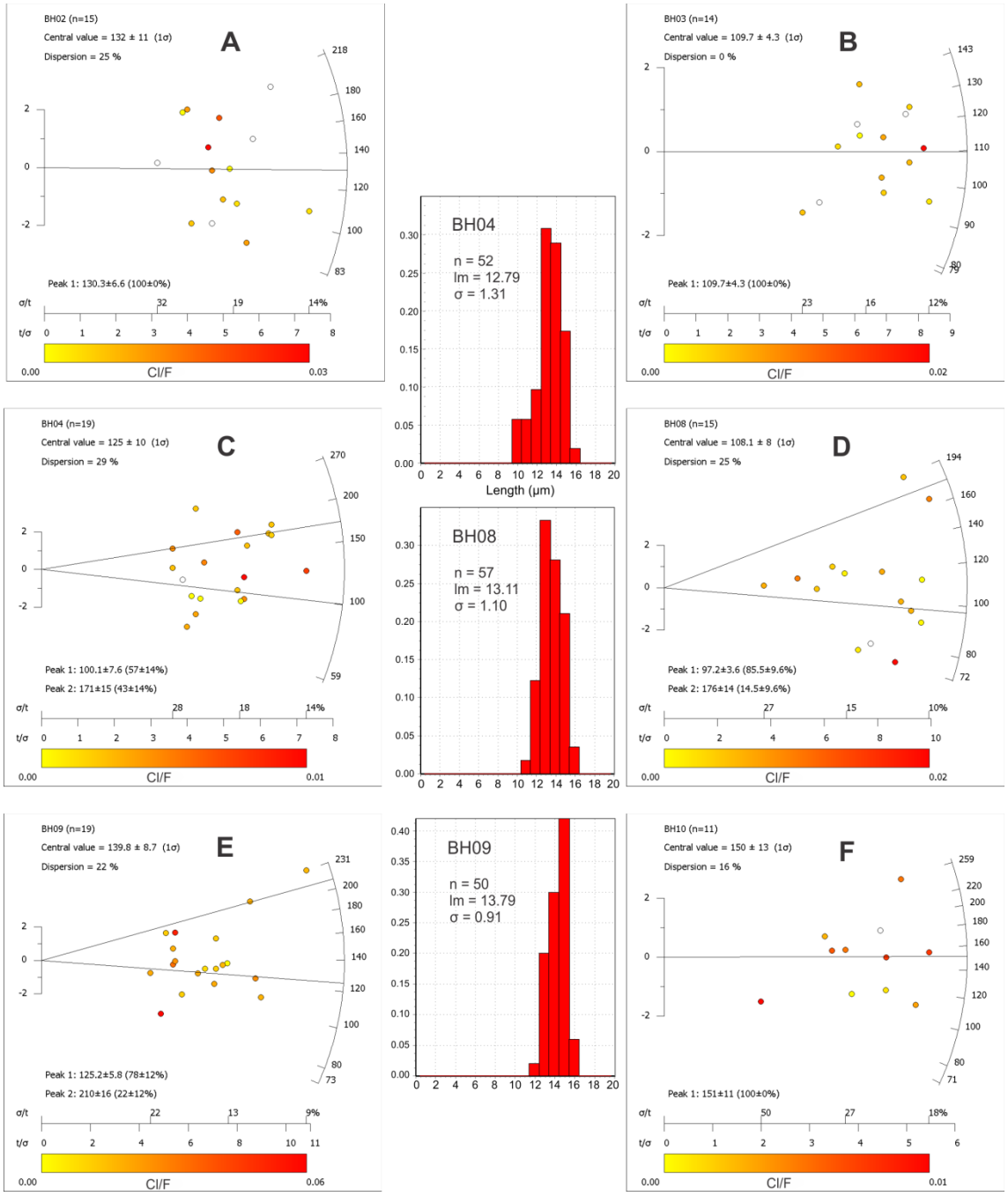

Figure 8: Radial plots of calculated AFT cooling ages for each sample location in the vicinity of Liuyuan (A-F). Central values were calculated and where the data shows a high degree of age dispersion (>20%) age-peak discrimination was performed using the automatic mixture model of the RadialPlotter software (Vermeesch 2009). The percentage of the data contained in each peak as well as age dispersion within each peak is shown in brackets with the age of each peak. Frequency plots depict length distribution of apatite fission tracks in samples from the area. n is the number of measured confined tracks, l_m is the average track length and σ is the standard deviation of the track lengths distribution.

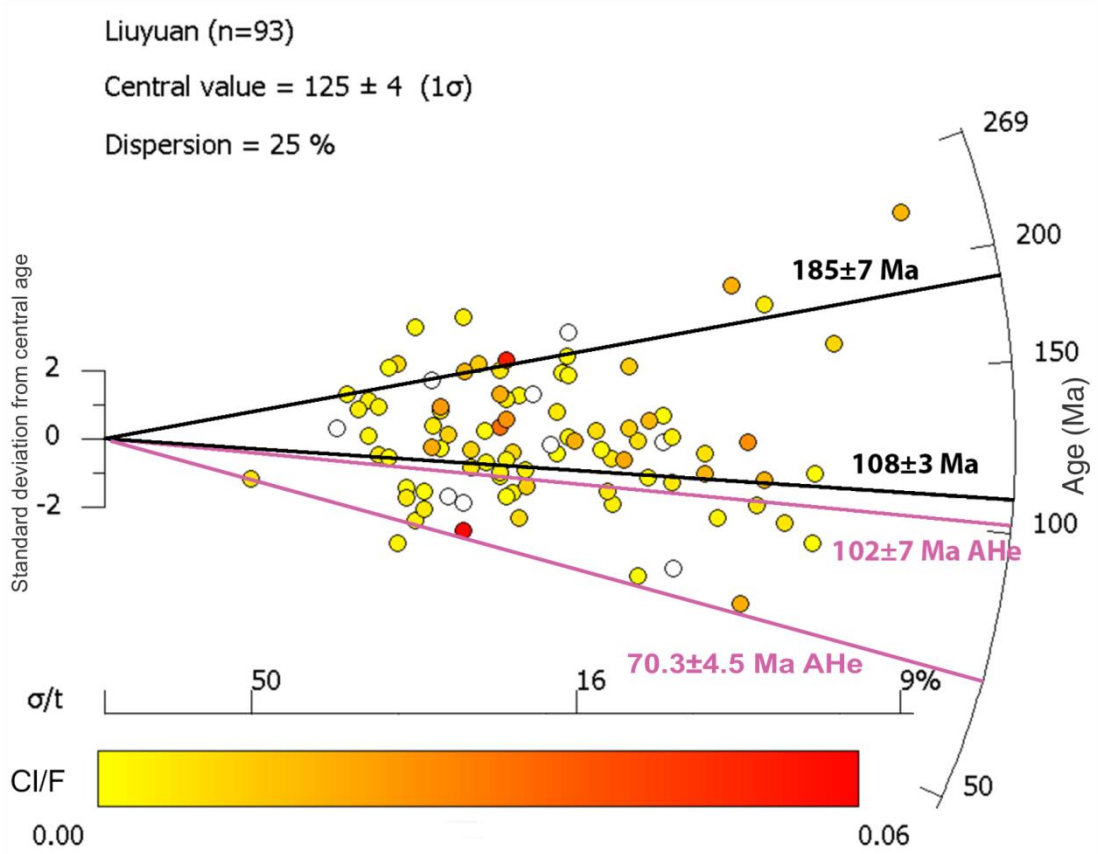

Figure 9: Radial plot of calculated AFT cooling ages combining all samples from the vicinity of Liuyuan. The data shows a high degree of dispersion (~25%) and therefore age-peak discrimination was performed using the automatic mixture model of the RadialPlotter software (Vermeesch 2009). Resultant age-peaks are shown in black. AHe ages are shown in pink and the older age mimics the younger of the two AFT age-peaks. Cl/F ratio is indicated by red/yellow colour scale.

The modelled thermal histories for the Liuyuan samples are generally similar to those from the Xingxingxia fault zone although the timing of cooling events differs slightly (Fig. 10). BH04 and BH08 show an initial period of slow cooling which is followed by an increased cooling rate at ~145-125 Ma for BH04 and ~125-105 Ma for BH08. This is followed by a moderate rate of cooling continuing to the present day. BH09 underwent rapid cooling at ~155-120 Ma before undergoing moderate to slow cooling into the present.

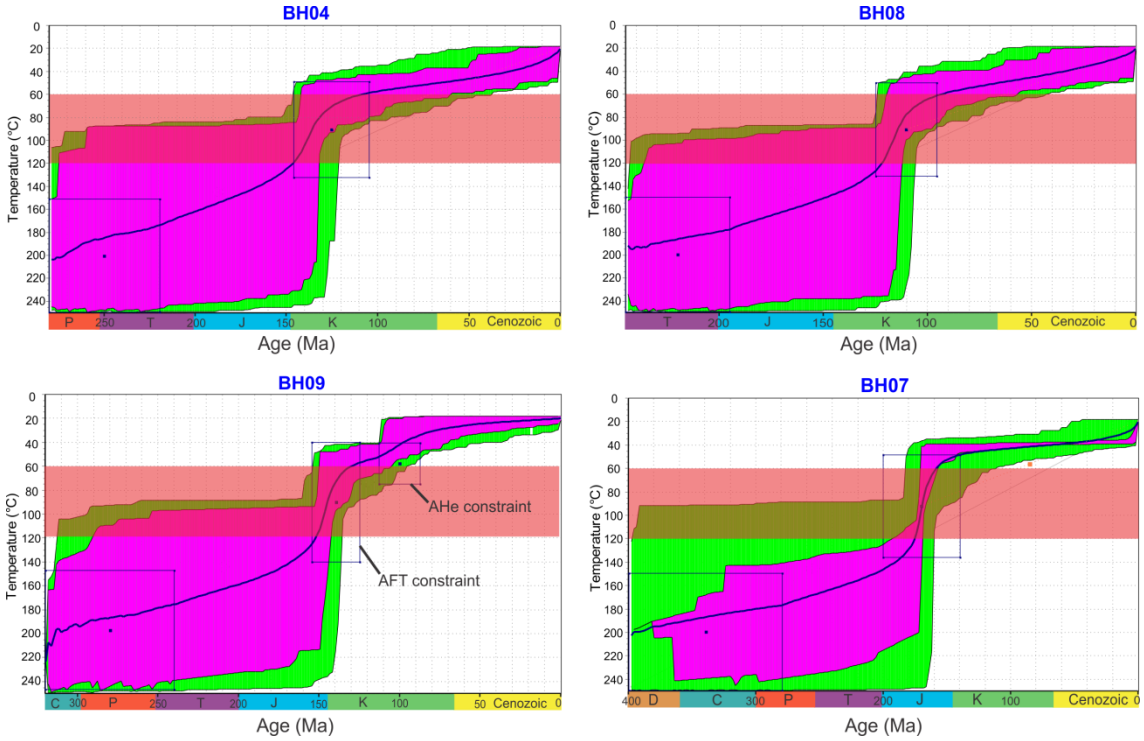

Figure 10: Thermal history models for samples in the vicinity of Liuyuan (BH04, BH08, BH09) and Dunhuang (BH07) generated using HeFTy software (Ketcham 2005). Modelling strategy uses box-constraints for AFT and AHe ages to generate paths of varying probability for the thermal history of the rock mass. The purple envelope encompasses 'Good' (>0.5) probability pathways and the green envelope 'Acceptable' (>0.05) pathways. The blue line represents the weighted mean path of the model. The Partial Annealing Zone (PAZ) is highlighted in red.

Dunhuang study area

The samples from the vicinity of Dunhuang yield central ages ranging from 141.4±9.9 Ma to 167.5±9.8 Ma (Figs. 11, 12). A combined plot of all the samples from the vicinity of Dunhuang (Fig. 12A) has a central age of 155.9±6.4 Ma. There is no apparent correlation between the age of an apatite grain and the Cl/F ratio of the grain in this plot. Only one sample yielded sufficient confined tracks to construct a length-distribution plot. The length distribution of sample BH07 gives a mean confined track length of 13.29µm and a standard deviation of 1.00µm which is indicative of fast cooling rates. AHe analysis of BH07 yielded ages of 126.8±8.4 Ma and 60.6.5±4.2 Ma, in comparison to age-peaks in the Dunhuang pooled radial plot at 192±8 Ma and 128±5 Ma. The

similarity of the younger AFT peak and the older AHe age is significant as it suggests an important cooling event occurred at ~130-120 Ma.

The thermal history model of BH07 suggests slow cooling until ~180 Ma, with rapid cooling until ~140 Ma, which was followed by thermal quiescence until the present (Fig. 10).

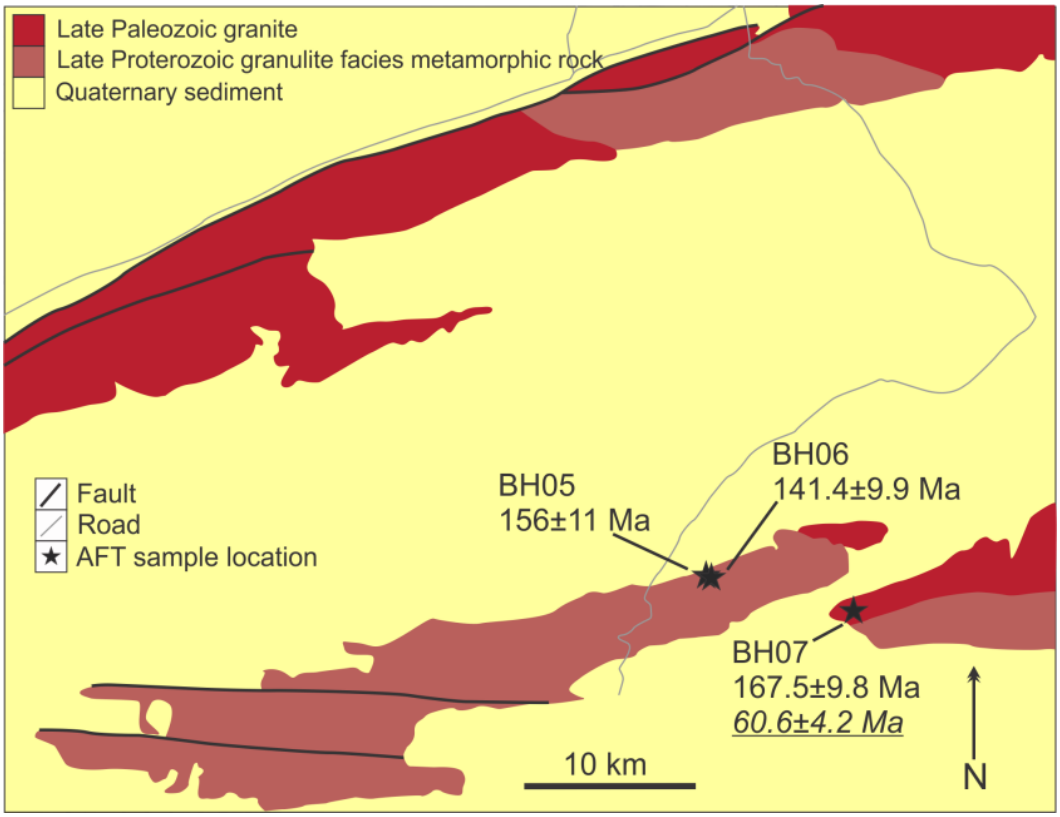

Figure 11: Map of sample area to the east of Dunhuang. AFT central ages and pooled AHe ages are from this study and are shown by star symbols. Modified after The Second Geological Team of the Gansu Bureau of Geology and Mineral Deposits 1967.

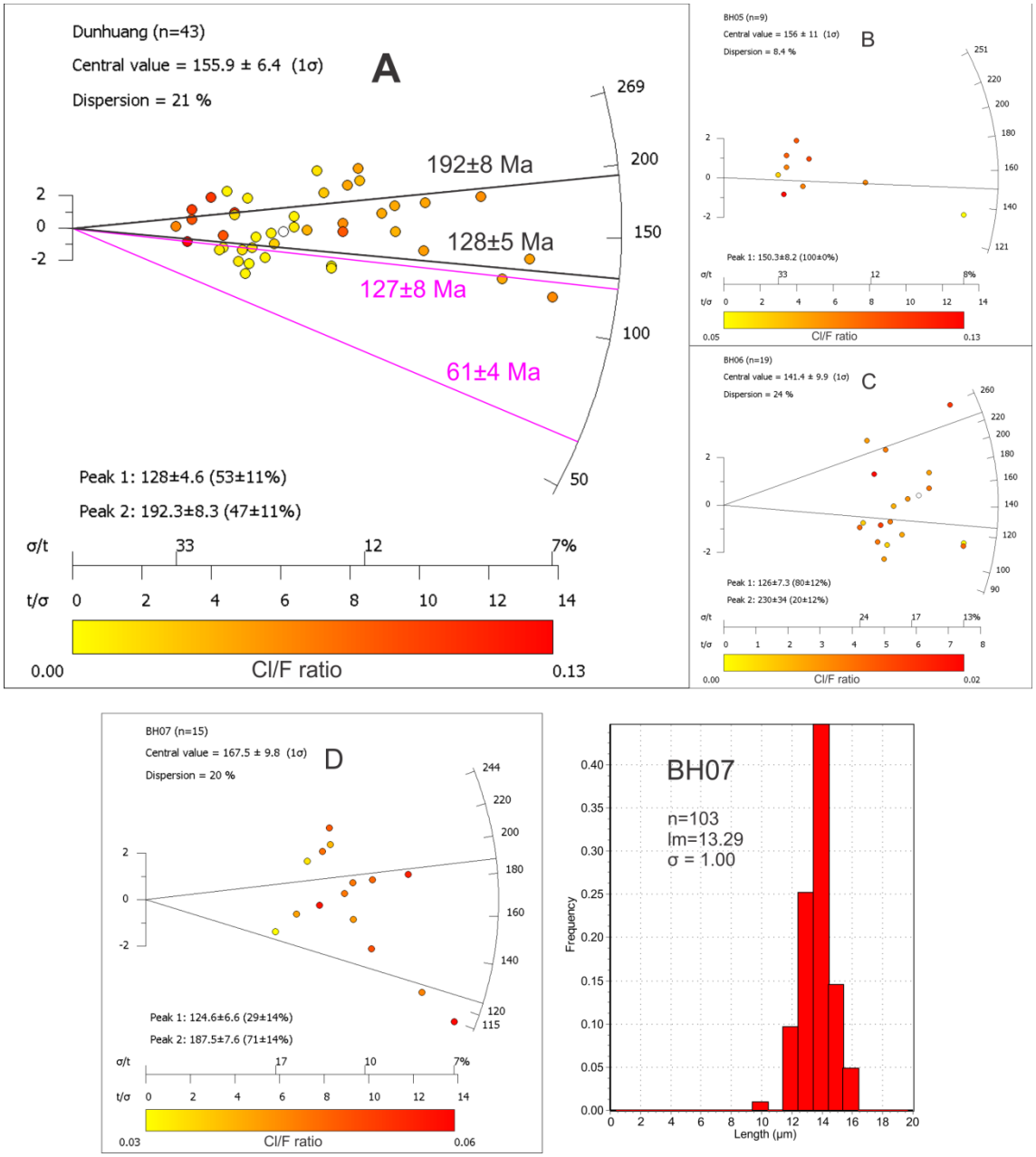

Figure 12: Radial plot of calculated AFT cooling ages combining all samples from the vicinity of Dunhuang (A) and individual plots for each sampling location (B-D). Central values were calculated and where the data shows a high degree of age dispersion (>20%) age-peak discrimination was performed using the automatic mixture model of the RadialPlotter software (Vermeesch 2009). The percentage of the data contained in each peak as well as age dispersion within each peak is shown in brackets with the age of each peak. Frequency plot depicts length distribution of apatite fission tracks in sample from the area. n is the number of measured confined tracks, l_m is the average track length and σ is the standard deviation of the track lengths distribution. AHe ages are shown in pink on the Dunhuang pooled plot and the older age mimics the younger of the two AFT age-peaks.

DISCUSSION

We interpret the thermochronological results obtained in this thesis as indicating widespread uplift in the Beishan during the Late Triassic- Early Jurassic (230-180 Ma) and middle Cretaceous (130-95 Ma). This is consistent with numerous other studies on the thermal history of the neighbouring regions (Dumitru *et al.,* 2001, Wang *et al.,* 2009, Glorie *et al.,* 2010, Jolivet *et al.,* 2010, De Grave *et al.,* 2011, Glorie *et al.,* 2011, De Grave *et al.,* 2012, De Grave *et al.,* 2013). Indeed, AFT basement cooling ages and detrital AFT age-populations from this period are prevalent throughout the CAOB as well as in neighbouring regions such as the Qilian Shan (George *et al.,* 2001, Jolivet *et al.,* 2001). Most authors interpret the Late Triassic – Early Jurassic cooling phase to be the result of intracontinental uplift and exhumation driven by the Late Triassic collision of the peri-Gondwanan Qiangtang block with the southern margin of Eurasia (e.g. Schwab *et al.,* 2004). The mid Cretaceous cooling phase can be linked with the collision of the peri-Gondwanan Lhasa block with the southern Eurasian margin or with the contemporaneous Mongol-Okhotsk Orogeny on the eastern Eurasian margin (e.g. Kapp *et al.,* 2007, Metelkin *et al.,* 2010). These events and their tectonic significance for the Beishan and the COAB as a whole are discussed in further detail below.

Late Triassic – Early Jurassic exhumation

The Late Triassic AFT age-peaks correspond well with previously obtained $^{40}Ar/^{39}Ar$ results of ~240-235 Ma (Wang *et al.,* 2010). Early to Middle Triassic ENE sinistral deformation in the Xingxingxia shear zone crosscuts a series of earlier E-W to NW-SE trending ductile shear zones that also occur throughout the Tianshan and Altai (Wang *et al.,* 2010). These early shear zones were active around 290-245 Ma and exploited inherited structures from the accretion of the region (Laurent-Charvet *et al.,* 2003). This

event accommodated the post-collisional eastwards extrusion of central Asia, potentially in response to the collision of the Tarim craton with Eurasia (Laurent-Charvet *et al.,* 2003, Allen *et al.,* 2006, Wang *et al.,* 2008). Shear kinematics of individual faults throughout the region over time were complex and varied, however importantly the final phase of deformation in the Tianshan from 250-245 Ma was dextral with a mainly E-W orientation (Laurent-Charvet *et al.,* 2003, Wang *et al.,* 2008). This late phase of deformation is relevant to the Beishan as Wang *et al.,* (2010) proposes that the Xingxingxia shear zone crosscuts and offsets this fabric. This relationship implies that the Beishan was once directly connected to the Tianshan (Wang *et al.,* 2010). The tectonic histories of the Beishan and the Tianshan were therefore closely linked until at least the middle Triassic, which explains why the Triassic exhumation pulse is very similar to that recorded in the Tianshan.

The lower limit on ductile deformation in the Xingxingxia shear zone is provided by the presence of a crosscutting granite intrusion dated to ca. 236 Ma (Wang *et al.,* 2010). However, several later phases of brittle deformation along the Xingxingxia shear zone and throughout the Beishan as a whole have been documented (Zheng *et al.,* 1996, Zhang and Cunningham 2012). Constraints on this later stage of brittle deformation are currently less robust, but stratigraphic and structural relationships have previously been interpreted to indicate that it probably occurred sometime between the middle Triassic and mid-Jurassic (Zheng *et al.,* 1996, Zhang and Cunningham 2012).

The collision/accretion of the Qiangtang block against the southern Eurasian margin coincides with recorded exhumation in the Beishan during the Late Triassic and Early

Jurassic (Fig. 13).

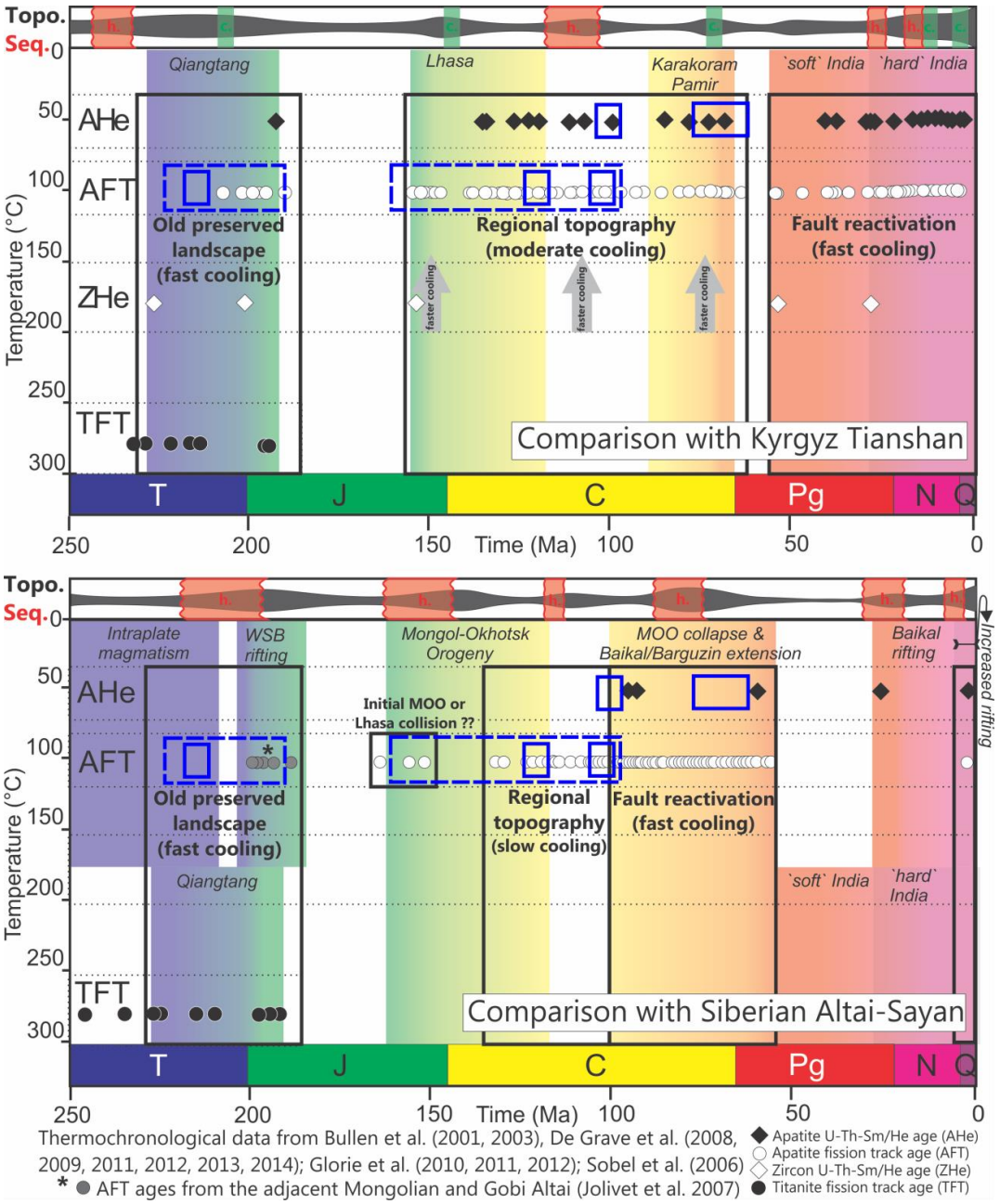

Figure 13: Comparison of the results obtained in this study (for the Beishan) with the thermochronological record of the Kyrgyz Tianshan and Siberian Altai-Sayan (modified after Glorie and De Grave., in preparation). The Beishan results are shown by blue boxes (solid = age peaks, dashed = spread in individual age data). The timing of the main tectonic events that affected the Tianshan and the Altai-Sayan are indicated as well. The upper panels for both figures show topography estimates (grey) based on the AFT data and simplified sequence stratigraphy (red and green) with h. = hiatus; c. = (alluvial) conglomerate: for the Tian Shan, the sequence stratigraphy constraints are based on data from the Tarim (Dumitru et al., 2001), Chu (Bullen et al., 2001) and Issyk-kul (Cobbold *et al.*, 1994) basins; for the Altai-Sayan based on data from the Kuznestk (Davies *et al.*, 2010), West-Siberian (Vyssotski *et al.*, 2006) and Chyua basins (Buslov et al., 1999).

Cretaceous exhumation

Mid Cretaceous (~130-95 Ma) rapid cooling was observed for the entire study area and indicates widespread exhumation throughout the BOC. The youngest AFT age-population (~100 Ma) of the Xingxingxia sample set, which is associated with high Cl/F ratios, suggests that exhumation and brittle reactivation of the Xingxingxia fault may have occurred well into the Cretaceous until around 100 Ma. This is in contrast with Zhang and Cunningham (2012) who concluded that brittle deformation in the Xingxingxia fault zone ceased much earlier, by the mid Jurassic at latest.

AHe ages closely mimic the AFT age-peaks when examining regional trends, which combined with the long mean track lengths suggests relatively rapid cooling during this period. Far-field stresses from the collision of the Cimmerian Lhasa terrane along the Bangong-Nujing suture in Tibet from 150-120 Ma (Kapp *et al.*, 2007, Leier *et al.*, 2007) is a possible cause for the Early Cretaceous uplift (Fig. 13). However, the widely observed ~100 Ma age-peak significantly postdates the Lhasa collision. Slab break-off during subduction of the Bangong-Nujing ocean plate at 105-100 Ma (Wu *et al.*, 2014) may provide the driving force for exhumation in the Beishan during the mid-Cretaceous. The main phase of the Mongol-Okhotsk Orogeny continues until around ~110 Ma (Fig. 13) and is also a possible driver for exhumation in the Beishan, though it occurs slightly earlier than the observed age-peaks (Jolivet *et al.*, 2010, Glorie *et al.*, 2012).

AHe ages from the Liuyuan area at 70.3±4.5 Ma and the Dunhuang area at 60.6±4.2 Ma suggest a latest Cretaceous – Paleogene cooling event in the south of the Beishan (Fig. 9, 12). The collision of the Karakorum block or the Kohistan-Dras island arc with Asia in modern day Pakistan/India (e.g. Glorie *et al.*, 2011) or plate reorganisation following

the collapse of the Mongol-Okhotsk Orogeny (e.g. Jolivet *et al.,* 2010, Glorie *et al.,* 2012) may be responsible for this uplift (Fig. 13).

Comparison with neighbouring regions

COMPARISON WITH EXHUMATION IN THE TIANSHAN AND SEDIMENTATION IN THE JUNGGAR AND TARIM BASINS

During the Mesozoic, the Tianshan experienced three main phases of exhumation, the Triassic-Early Jurassic, the Early Cretaceous and the Late Cretaceous. The late Triassic – early Jurassic AFT ages obtained for the BOC correspond well with data previously obtained for the Tianshan that are usually associated with stress propagation from the Qiangtang collision (Fig. 5,9,12; Jolivet *et al.,* 2010, De Grave *et al.,* 2011).

Triassic – Early Jurassic exhumation is less commonly observed compared to the Cretaceous exhumation phases, although they have been found in the Kyrgyz Tianshan (De Grave *et al.,* 2011, Glorie *et al.,* 2011) as well as the Chinese Tianshan (Dumitru *et al.,* 2001, Jolivet *et al.,* 2010). Most of these ages were obtained on detrital sediments that are the erosion products of more ancient relief, as well as on old preserved landscape features such as internally drained plateaus (De Grave *et al.,* 2011). The oldest age-peaks in our Beishan data correlate well with this time period, although no central ages or tT models indicate significant cooling prior to the Late Jurassic (Fig. 13). Evidence of this exhumation has likely been eroded due to later uplift in combination with unfavourable conditions for preservation.

Throughout the Kyrgyz and Chinese Tianshan we see strong evidence for Late Jurassic-Cretaceous exhumation (Bullen *et al.,* 2001, Dumitru *et al.,* 2001, Sobel *et al.,* 2006, De Grave *et al.,* 2007, Wang *et al.,* 2009, Zhang *et al.,* 2009, Glorie *et al.,* 2010, Jolivet *et al.,* 2010, De Grave *et al.,* 2011, Glorie *et al.,* 2011, De Grave *et al.,* 2012, De Grave *et*

al., 2013). Ages from basement rocks in the Tianshan and from detrital samples in nearby basins provide a detailed and comprehensive record of the Cretaceous exhumation episode (Fig. 13). Sedimentological analysis further confirms that an ancient mountain range existed during this time period, separating the Tarim and Junggar basins (Hendrix 2000). Phases of uplift occurring around ~150 Ma and ~120 Ma are also reflected in our results which also show cooling in the Beishan at this time. Our results show further cooling to around 100 Ma, which is also common in the Tianshan.

Extensive Mesozoic sedimentation to the east of the Beishan is further evidence for exhumation (Fig. 1). Largely Cretaceous shallow marine sedimentation is accompanied by some minor Jurassic sedimentation. The Cretaceous units include abundant sandstones and some conglomerates suggesting a proximal source of sediment. This is consistent with reported Early Cretaceous sandstones and conglomerates in the Tarim and Junggar basins which lie on either side of the Tianshan, and which have been linked to this phase of exhumation (Dumitru *et al.*, 2001, Jolivet *et al.*, 2010).

During the Late Cretaceous – Early Paleogene the Tianshan experienced localised exhumation along fault zones that coincides with AHe ages found in the Beishan (Glorie *et al.*, 2011).

COMPARISON WITH THE ALTAI-SAYAN

To the north and north east, the Siberian and Gobi Altai have yielded comparable results to this study (Vassallo *et al.*, 2007, Jolivet *et al.*, 2009, Glorie *et al.*, 2012). The same three phases of Mesozoic-Paleogene uplift recorded in the Tianshan are present in the Altai, though the intensity and exact timing of each phase differs (Fig. 13). Due to the proximity of the Altai to the Mongol-Okhotsk suture, uplift and exhumation in the Altai

is frequently attributed to the Mongol-Okhotsk Orogeny rather than to the Cimmerian Orogeny. The various stages of the Mongol-Okhotsk Orogeny (Metelkin *et al.*, 2010) including the Late Triassic - Early Jurassic initiation, the Late Jurassic - Early Cretaceous main phase and the Late Cretaceous - Early Paleogene collapse have been used to explain the three phases of contemporaneous exhumation in the Altai, and as discussed, may also have contributed to exhumation in the Beishan (Fig. 13; Yuan *et al.*, 2006, Vassallo *et al.*, 2007, Jolivet *et al.*, 2009, Glorie *et al.*, 2012, De Grave *et al.*, 2014).

The effect of the Mongol-Okhotsk Orogeny on the development of the Tianshan has also been discussed but it is difficult to differentiate between the effects of the Cimmerian and Mongol-Okhotsk Orogeny due to the fact that they occurred at the same time (Jolivet *et al.*, 2010). Given the proximity of the Beishan to both the Lhasa and Mongol-Okhotsk suture, it is very likely that both the collision of the Lhasa block with the southern margin of Eurasia and the Mongol-Okhotsk Orogeny influenced the development of the Beishan in the 150-100 Ma period where we found the majority of the uplift to have occurred.

Late Cenozoic exhumation in the CAOB

The Beishan had a similar history to surrounding mountains ranges until the earliest Paleogene, after which the Tianshan, Qilian-shan and Altai all underwent at least one major phase of modern deformation in response to the India-Asia collision. The Qilian-shan experienced uplift and exhumation beginning at around 40-35 Ma, the Tianshan at ~35-30 Ma and the Altai at ~8-5 Ma, reflecting the northwards propagation of the stress from the India-Eurasia collision zone (Vassallo *et al.*, 2007). Early exhumation in the Qilianshan and Tianshan (>25 Ma) is less profound and may reflect the influence of the

'soft' collision of Greater India with Eurasia, which involved the subduction of extended crust and oceanic lithosphere (van Hinsbergen *et al.*, 2012). The 'hard' India-Eurasia collision involving thick crust at ~25 Ma induced a much stronger phase of uplift which is seen in the thermochronological record throughout the CAOB (Vassallo *et al.*, 2007, Glorie *et al.*, 2012, De Grave *et al.*, 2013). In the Beishan, no evidence for these events can be found in the thermochronological record. The reason for this divergence between the history of the Beishan and the surrounding mountains is not yet clear. The Tianshan progressively decreases in height towards the east, and the Beishan itself lies immediately to the south-east of the lowest of the Tianshan ranges. Samples from these mountains are currently undergoing analysis, which may shed light on the dynamics of the modern uplift of the eastern Tianshan and provide an explanation for this trend. This in turn may provide answers for remaining questions about the thermal history of the Beishan, especially with regard to the lack of evidence for Late Cenozoic exhumation in the this region.

CONCLUSIONS

Low temperature thermochronological results from the BOC reveal three main phases of exhumation which largely mimic the thermal history of nearby mountain ranges in the CAOB

I. AFT age-peaks suggest early exhumation during the Late Triassic - Early Jurassic (230-180 Ma) linked with the Qiangtang collision.

II. AFT age-peaks and AHe ages in combination with thermal history modelling reveal a main phase of uplift during the early-mid Cretaceous (130-95 Ma) corresponding to the Lhasa collision and subsequent slab break-off or to the Mongol-Okhotsk Orogeny and subsequent collapse. Brittle reactivation of inherited structures may continue to play a role in this phase of exhumation contrary to the conclusions of past studies.

III. AHe ages point to a Late Cretaceous-Early Paleogene event in the south of the BOC (~70-60 Ma) in response to the Karakorum block or Kohistan-Dras arc collision.

No evidence was found for any exhumation in response to the India-Asia collision in the Cenozoic, which is a significant point of difference from the thermal histories of the surrounding mountain ranges. Further thermochronology and structural studies of the Beishan and the eastern Tianshan may help explain this discrepancy.

ACKNOWLEDGMENTS

I give thanks to Stijn Glorie and Alan Collins, my supervisors, for their guidance and endless patience. Ros King and Katie Howard supported the entire Honours cohort throughout the year with information sessions and advice. This work was financially supported by the 973 Program (2014CB440801), the National Science Foundation of China (grants #41230207 and #41302167) and the IGCP project 592. The support of the Australian Government through the 2014 Prime Minister's Australia Asia Endeavour Scholarship was also instrumental in the success of this work. Adelaide Microscopy,

and in particular Benjamin Wade, helped me immensely with the use of the LA-ICP-MS. Noreen Evans and Bradley McDonald performed AHe analysis. I thank Song Dongfang for field assistance and Morgan Blades for advice and assistance in the lab.

REFERENCES

ALLEN M. B., ANDERSON L., SEARLE R. C. & BUSLOV M. 2006 Oblique rift geometry of the West Siberian Basin: tectonic setting for the Siberian flood basalts, *Journal of the Geological Society,* vol. 163, no. 6, 901-904.

BULLEN M. E., BURBANK D. W., GARVER J. I. & ABDRAKHMATOV K. Y. 2001 Late Cenozoic tectonic evolution of the northwestern Tien Shan: New age estimates for the initiation of mountain building, *Geological Society of America Bulletin,* vol. 113, no. 12, 1544-1559.

COBBOLD P. R., SADYBAKASOV E. & THOMAS J. C. 1994 Cenozoic transpression and basin development, Kyrghyz Tienshan, Central Asia. In ROURE F.*, et al.* eds. Geodynamic Evolution of Sedimentary Basins. International Symposium*.* pp. 181-202. Moscow.

CTAJ 2007 Chinese Tianshan and its Adjacent Area 1 : 1 000 000. In BUREAU X. A. G. S. C. O. C. G. S. ed. Beijing: Geological Publishing House.

DAVIES C., ALLEN M. B., BUSLOV M. M. & SAFONOVA I. 2010 Deposition in the Kuznetsk Basin, Siberia: Insights into the Permian–Triassic transition and the Mesozoic evolution of Central Asia, *Palaeogeography, Palaeoclimatology, Palaeoecology,* vol. 295, no. 1–2, 307-322.

DE GRAVE J., BUSLOV M. M. & VAN DEN HAUTE P. 2007 Distant effects of India–Eurasia convergence and Mesozoic intracontinental deformation in Central Asia: Constraints from apatite fission-track thermochronology, *Journal of Asian Earth Sciences,* vol. 29, no. 2–3, 188-204.

DE GRAVE J., GLORIE S., BUSLOV M. M., IZMER A., FOURNIER-CARRIE A., BATALEV V. Y., VANHAECKE F., ELBURG M. & VAN DEN HAUTE P. 2011 The thermo-tectonic history of the Song-Kul plateau, Kyrgyz Tien Shan: Constraints by apatite and titanite thermochronometry and zircon U/Pb dating, *Gondwana Research,* vol. 20, no. 4, 745-763.

DE GRAVE J., GLORIE S., RYABININ A., ZHIMULEV F., BUSLOV M. M., IZMER A., ELBURG M., VANHAECKE F. & VAN DEN HAUTE P. 2012 Late Palaeozoic and Meso-Cenozoic tectonic evolution of the southern Kyrgyz Tien Shan: Constraints from multi-method thermochronology in the Trans-Alai, Turkestan-Alai segment and the southeastern Ferghana Basin, *Journal of Asian Earth Sciences,* vol. 44, no. 0, 149-168.

DE GRAVE J., GLORIE S., BUSLOV M. M., STOCKLI D. F., MCWILLIAMS M. O., BATALEV V. Y. & VAN DEN HAUTE P. 2013 Thermo-tectonic history of the Issyk-Kul basement (Kyrgyz Northern Tien Shan, Central Asia), *Gondwana Research,* vol. 23, no. 3, 998-1020.

DE GRAVE J., DE PELSMAEKER E., ZHIMULEV F. I., GLORIE S., BUSLOV M. M. & VAN DEN HAUTE P. 2014 Meso-Cenozoic building of the northern Central Asian Orogenic Belt: Thermotectonic history of the Tuva region, *Tectonophysics,* vol. 621, no. 0, 44-59.

DUMITRU T. A., ZHOU D., CHANG E. Z., GRAHAM S. A., HENDRIX M. S., SOBEL E. R. & CARROLL A. R. 2001 Uplift, exhumation, and deformation in the Chinese Tian Shan, *Geological Society of America Memoirs,* vol. 194, 71-99.

EHLERS T. A. & FARLEY K. A. 2003 Apatite (U–Th)/He thermochronometry: methods and applications to problems in tectonic and surface processes, *Earth and Planetary Science Letters,* vol. 206, no. 1–2, 1-14.

EVANS N. J., BYRNE J. P., KEEGAN J. T. & DOTTER L. E. 2005 Determination of Uranium and Thorium in Zircon, Apatite, and Fluorite: Application to Laser (U-Th)/He Thermochronology, *Journal of Analytical Chemistry,* vol. 60, no. 12, 1159-1165.

GEORGE A. D., MARSHALLSEA S. J., WYRWOLL K.-H., JIE C. & YANCHOU L. 2001 Miocene cooling in the northern Qilian Shan, northeastern margin of the Tibetan Plateau, revealed by apatite fission-track and vitrinite-reflectance analysis, *Geology,* vol. 29, no. 10, 939-942.

GLEADOW A. J. W., DUDDY I. R., GREEN P. F. & HEGARTY K. A. 1986a Fission track lengths in the apatite annealing zone and the interpretation of mixed ages, *Earth and Planetary Science Letters,* vol. 78, no. 2–3, 245-254.

GLEADOW A. J. W., DUDDY I. R., GREEN P. F. & LOVERING J. F. 1986b Confined fission track lengths in apatite: a diagnostic tool for thermal history analysis, *Contributions to Mineralogy and Petrology,* vol. 94, no. 4, 405-415.

GLORIE S., DE GRAVE J., BUSLOV M. M., ELBURG M. A., STOCKLI D. F., GERDES A. & VAN DEN HAUTE P. 2010 Multi-method chronometric constraints on the evolution of the Northern Kyrgyz Tien Shan granitoids (Central Asian Orogenic Belt): From emplacement to exhumation, *Journal of Asian Earth Sciences,* vol. 38, no. 3–4, 131-146.

GLORIE S., DE GRAVE J., BUSLOV M. M., ZHIMULEV F. I., STOCKLI D. F., BATALEV V. Y., IZMER A., VAN DEN HAUTE P., VANHAECKE F. & ELBURG M. A. 2011 Tectonic history of the Kyrgyz South Tien Shan (Atbashi-Inylchek) suture zone: The role of inherited structures during deformation-propagation, *Tectonics,* vol. 30, no. 6, p. TC6016.

GLORIE S., DE GRAVE J., BUSLOV M. M., ZHIMULEV F. I., ELBURG M. A. & VAN DEN HAUTE P. 2012 Structural control on Meso-Cenozoic tectonic reactivation and denudation in the Siberian Altai: Insights from multi-method thermochronometry, *Tectonophysics,* vol. 544–545, no. 0, 75-92.

GREEN P. F., DUDDY I. R., GLEADOW A. J. W., TINGATE P. R. & LASLETT G. M. 1986 Thermal annealing of fission tracks in apatite: 1. A qualitative description, *Chemical Geology: Isotope Geoscience section,* vol. 59, no. 0, 237-253.

HASEBE N., BARBARAND J., JARVIS K., CARTER A. & HURFORD A. J. 2004 Apatite fission-track chronometry using laser ablation ICP-MS, *Chemical Geology,* vol. 207, no. 3–4, 135-145.

HENDRIX M. S. 2000 Evolution of Mesozoic Sandstone Compositions, Southern Junggar, Northern Tarim, and Western Turpan Basins, Northwest China: A Detrital Record of the Ancestral Tian Shan, *Journal of Sedimentary Research,* vol. 70, no. 3, 520-532.

JOLIVET M., BRUNEL M., SEWARD D., XU Z., YANG J., ROGER F., TAPPONNIER P., MALAVIEILLE J., ARNAUD N. & WU C. 2001 Mesozoic and Cenozoic tectonics of the northern edge of the Tibetan plateau: fission-track constraints, *Tectonophysics,* vol. 343, no. 1–2, 111-134.

JOLIVET M., DE BOISGROLLIER T., PETIT C., FOURNIER M., SANKOV V. A., RINGENBACH J. C., BYZOV L., MIROSHNICHENKO A. I., KOVALENKO S. N. & ANISIMOVA S. V. 2009 How old is the Baikal Rift Zone? Insight from apatite fission track thermochronology, *Tectonics,* vol. 28, no. 3, p. TC3008.

JOLIVET M., DOMINGUEZ S., CHARREAU J., CHEN Y., LI Y. & WANG Q. 2010 Mesozoic and Cenozoic tectonic history of the central Chinese Tian Shan: Reactivated tectonic structures and active deformation, *Tectonics,* vol. 29, no. 6, p. TC6019.

KAPP P., DECELLES P. G., GEHRELS G. E., HEIZLER M. & DING L. 2007 Geological records of the Lhasa-Qiangtang and Indo-Asian collisions in the Nima area of central Tibet, *Geological Society of America Bulletin,* vol. 119, no. 7-8, 917-933.

KETCHAM R. A., DONELICK R. A. & CARLSON W. D. 1999 Variability of apatite fission-track annealing kinetics; III, Extrapolation to geological time scales, *American Mineralogist,* vol. 84, no. 9, 1235-1255.

KETCHAM R. A. 2005 Forward and Inverse Modeling of Low-Temperature Thermochronometry Data, *Reviews in Mineralogy and Geochemistry,* vol. 58, no. 1, 275-314.

KHAIN E. V., BIBIKOVA E. V., KRÖNER A., ZHURAVLEV D. Z., SKLYAROV E. V., FEDOTOVA A. A. & KRAVCHENKO-BEREZHNOY I. R. 2002 The most ancient ophiolite of the Central Asian fold belt: U–Pb and Pb–Pb zircon ages for the Dunzhugur Complex, Eastern Sayan, Siberia, and geodynamic implications, *Earth and Planetary Science Letters,* vol. 199, no. 3–4, 311-325.

LAURENT-CHARVET S., CHARVET J., MONIÉ P. & SHU L. 2003 Late Paleozoic strike-slip shear zones in eastern central Asia (NW China): New structural and geochronological data, *Tectonics,* vol. 22, no. 2, p. 1009.

LEIER A. L., DECELLES P. G., KAPP P. & GEHRELS G. E. 2007 Lower Cretaceous Strata in the Lhasa Terrane, Tibet, with Implications for Understanding the Early Tectonic History of the Tibetan Plateau, *Journal of Sedimentary Research,* vol. 77, no. 10, 809-825.

LIU Y., GENSER J., NEUBAUER F., JIN W., GE X., HANDLER R. & TAKASU A. 2005 40Ar/39Ar mineral ages from basement rocks in the Eastern Kunlun Mountains, NW China, and their tectonic implications, *Tectonophysics,* vol. 398, no. 3–4, 199-224.

MACAULAY E. A., SOBEL E. R., MIKOLAICHUK A., KOHN B. & STUART F. M. 2014 Cenozoic deformation and exhumation history of the Central Kyrgyz Tien Shan, *Tectonics,* vol. 33, no. 2, p. 2013TC003376.

METELKIN D. V., VERNIKOVSKY V. A., KAZANSKY A. Y. & WINGATE M. T. D. 2010 Late Mesozoic tectonics of Central Asia based on paleomagnetic evidence, *Gondwana Research,* vol. 18, no. 2–3, 400-419.

SCHWAB M., RATSCHBACHER L., SIEBEL W., MCWILLIAMS M., MINAEV V., LUTKOV V., CHEN F., STANEK K., NELSON B., FRISCH W. & WOODEN J. L. 2004 Assembly of the Pamirs: Age and origin of magmatic belts from the southern Tien Shan to the southern Pamirs and their relation to Tibet, *Tectonics,* vol. 23, no. 4, p. TC4002.

SENGOR A. M. C., NATAL'IN B. A. & BURTMAN V. S. 1993 Evolution of the Altaid tectonic collage and Palaeozoic crustal growth in Eurasia, *Nature,* vol. 364, no. 6435, 299-307.

SOBEL E. R., OSKIN M., BURBANK D. & MIKOLAICHUK A. 2006 Exhumation of basement-cored uplifts: Example of the Kyrgyz Range quantified with apatite fission track thermochronology, *Tectonics,* vol. 25, no. 2, p. TC2008.

VAN HINSBERGEN D. J. J., LIPPERT P. C., DUPONT-NIVET G., MCQUARRIE N., DOUBROVINE P. V., SPAKMAN W. & TORSVIK T. H. 2012 Greater India Basin hypothesis and a two-stage Cenozoic collision between India and Asia, *Proceedings of the National Academy of Sciences,* vol. 109, no. 20, 7659-7664.

VASSALLO R., JOLIVET M., RITZ J. F., BRAUCHER R., LARROQUE C., SUE C., TODBILEG M. & JAVKHLANBOLD D. 2007 Uplift age and rates of the Gurvan Bogd system (Gobi-Altay) by apatite fission track analysis, *Earth and Planetary Science Letters,* vol. 259, no. 3–4, 333-346.

VERMEESCH P. 2009 RadialPlotter: a Java application for fission track, luminescence and other radial plots. Radiation Measurements.

VYSSOTSKI A. V., VYSSOTSKI V. N. & NEZHDANOV A. A. 2006 Evolution of the West Siberian Basin, *Regional Geology and Tectonics*, 754-801.

WAGNER G. A., GLEADOW A. J. W. & FITZGERALD P. G. 1989 The significance of the partial annealing zone in apatite fission-track analysis: Projected track length measurements and uplift chronology of the transantarctic mountains, *Chemical Geology: Isotope Geoscience section,* vol. 79, no. 4, 295-305.

WANG Q., LI S. & DU Z. 2009 Differential uplift of the Chinese Tianshan since the Cretaceous: constraints from sedimentary petrography and apatite fission-track dating, *International Journal of Earth Sciences,* vol. 98, no. 6, 1341-1363.

WANG Y., ZHANG X., WANG E., ZHANG J., LI Q. & SUN G. 2005 40Ar/39Ar thermochronological evidence for formation and Mesozoic evolution of the northern-central segment of the Altyn Tagh fault system in the northern Tibetan Plateau, *Geological Society of America Bulletin,* vol. 117, no. 9-10, 1336-1346.

WANG Y., LI J. & SUN G. 2008 Postcollisional Eastward Extrusion and Tectonic Exhumation along the Eastern Tianshan Orogen, Central Asia: Constraints from Dextral Strike-Slip Motion and 40Ar/39Ar Geochronological Evidence, *Journal of Geology,* vol. 116, no. 6, 599-618.

WANG Y., SUN G. & LI J. 2010 U-Pb (SHRIMP) and 40Ar/39Ar geochronological constraints on the evolution of the Xingxingxia shear zone, NW China: A Triassic segment of the Altyn Tagh fault system, *Geological Society of America Bulletin,* vol. 122, no. 3-4, 487-505.

WINDLEY B. F., ALEXEIEV D., XIAO W., KRÖNER A. & BADARCH G. 2007 Tectonic models for accretion of the Central Asian Orogenic Belt, *Journal of the Geological Society,* vol. 164, no. 1, 31-47.

WU H., LI C., HU P. & LI X. 2014 Early Cretaceous (100–105 Ma) Adakitic magmatism in the Dachagou area, northern Lhasa terrane, Tibet: implications for the Bangong–Nujiang Ocean subduction and slab break-off, *International Geology Review*, 1-17.

XIAO W., WINDLEY B. F., HAO J. & ZHAI M. 2003 Accretion leading to collision and the Permian Solonker suture, Inner Mongolia, China: Termination of the central Asian orogenic belt, *Tectonics,* vol. 22, no. 6, p. 1069.

XIAO W. J., WINDLEY B. F., HUANG B. C., HAN C. M., YUAN C., CHEN H. L., SUN M., SUN S. & LI J. L. 2009a End-Permian to mid-Triassic termination of the accretionary processes of the southern Altaids: implications for the geodynamic evolution, Phanerozoic continental growth, and metallogeny of Central Asia, *International Journal of Earth Sciences,* vol. 98, no. 6, 1189-1217.

XIAO W. J., WINDLEY B. F., YUAN C., SUN M., HAN C. M., LIN S. F., CHEN H. L., YAN Q. R., LIU D. Y., QIN K. Z., LI J. L. & SUN S. 2009b Paleozoic multiple subduction-accretion processes of the southern Altaids, *American Journal of Science,* vol. 309, no. 3, 221-270.

XIAO W. J., MAO Q. G., WINDLEY B. F., HAN C. M., QU J. F., ZHANG J. E., AO S. J., GUO Q. Q., CLEVEN N. R., LIN S. F., SHAN Y. H. & LI J. L. 2010 Paleozoic multiple accretionary and collisional processes of the Beishan orogenic collage, *American Journal of Science,* vol. 310, no. 10, 1553-1594.

YUAN W., CARTER A., DONG J., BAO Z., AN Y. & GUO Z. 2006 Mesozoic–Tertiary exhumation history of the Altai Mountains, northern Xinjiang, China: New constraints from apatite fission track data, *Tectonophysics,* vol. 412, no. 3–4, 183-193.

ZHANG J. & CUNNINGHAM D. 2012 Kilometer-scale refolded folds caused by strike-slip reversal and intraplate shortening in the Beishan region, China, *Tectonics,* vol. 31, no. 3, p. TC3009.

ZHANG L., AI Y., LI X., RUBATTO D., SONG B., WILLIAMS S., SONG S., ELLIS D. & LIOU J. G. 2007 Triassic collision of western Tianshan orogenic belt, China: Evidence from SHRIMP U–Pb dating of zircon from HP/UHP eclogitic rocks, *Lithos,* vol. 96, no. 1–2, 266-280.

ZHANG Z., ZHU W., SHU L., WAN J., YANG W., SU J. & ZHENG B. 2009 Apatite fission track thermochronology of the Precambrian Aksu blueschist, NW China: Implications for thermo–tectonic evolution of the north Tarim basement, *Gondwana Research,* vol. 16, no. 2, 182-188.

ZHENG Y., ZHANG Q., WANG Y., LIU R., WANG S. G., ZUO G., WANG S. Z., LKAASUREN B., BADARCH G. & BADAMGARAV Z. 1996 Great Jurassic thrust sheets in Beishan (North Mountains)—Gobi areas of China and southern Mongolia, *Journal of Structural Geology,* vol. 18, no. 9, 1111-1126.

APPENDIX A: DATA TABLE

Data reduction table combining LA-ICP-MS data and AFT counting data to produce ages that are used in RadialPlotter software.

Sample	Measured ^{238}U	SD %	Measured ^{44}Ca	SD %	Measured $^{238}U/^{44}Ca$	SD %	^{238}U Dur	RF	SD	N_s	A	ρ_s	t (Ma)	SD t
BH01 - 1	5248.590	2.199	1634529.586	2.109	0.0032	0.762	8.116	0.822	0.067	41	4800	854166.7	**237.52**	37.15
BH01 - 2	10427.887	1.011	1873616.673	0.809	0.0056	0.581	14.007	0.658	0.092	28	6000	466666.7	**76.14**	14.40
BH01 - 3	9579.248	0.976	1841629.917	0.882	0.0052	0.451	13.051	0.547	0.071	75	10000	750000	**130.78**	15.12
BH01 - 4	8662.719	0.954	2215717.147	0.716	0.0039	1.266	9.604	1.303	0.125	22	3600	611111.1	**144.65**	30.90
BH01 - 5	5099.837	1.961	1929443.484	1.607	0.0026	0.831	6.594	0.886	0.058	15	4000	375000	**129.44**	33.44
BH01 - 6	12496.224	1.314	1866232.144	0.973	0.0067	0.597	17.170	0.673	0.116	72	7000	1028571	**136.28**	16.09
BH01 - 7	11218.174	1.515	1758771.195	0.789	0.0063	0.866	16.113	0.920	0.148	24	2500	960000	**135.54**	27.69
BH01 - 8	18228.574	0.877	1851378.904	0.575	0.0099	0.930	25.137	0.981	0.247	51	6300	809523.8	**73.62**	10.33
BH01 - 9	16762.272	1.900	1753986.137	1.370	0.0095	0.735	23.929	0.801	0.192	78	7200	1083333	**103.25**	11.72
BH01 - 11	16896.245	0.853	1794202.344	0.650	0.0094	0.420	23.789	0.529	0.126	75	7000	1071429	**102.72**	11.87
BH01 - 12	15350.680	0.620	1849844.016	0.647	0.0083	0.482	20.944	0.580	0.121	38	5000	760000	**82.89**	13.46
BH01 - 16	7522.060	0.908	1862361.087	0.747	0.0040	0.516	10.200	0.611	0.062	32	6400	500000	**111.72**	19.76
BH01 - 18	13499.195	0.562	1773220.028	0.486	0.0076	0.407	19.303	0.531	0.103	97	8000	1212500	**142.81**	14.52
BH01 - 19	10937.770	2.117	1699970.695	1.343	0.0064	1.353	16.113	1.396	0.225	44	4800	916666.7	**129.48**	19.60
BH02 - 01	12181.203	0.960	1690352.832	0.837	0.0072	0.655	17.948	0.741	0.133	25	3000	833333.3	**105.87**	21.19
BH02 - 04	13784.945	0.875	1776772.397	0.730	0.0078	0.407	19.742	0.538	0.106	34	2500	1360000	**156.47**	26.85
BH02 - 05	11793.891	0.913	1595681.651	0.906	0.0074	0.501	18.467	0.622	0.115	22	2100	1047619	**129.12**	27.54
BH02 - 06	12690.457	0.807	1823465.110	0.855	0.0070	0.777	17.545	0.861	0.151	32	5000	640000	**83.32**	14.75
BH02 - 07	37972.667	0.850	1953887.956	0.984	0.0195	0.756	48.563	0.843	0.409	55	2400	2291667	**107.59**	14.54
BH02 - 08	13684.628	1.492	1505530.754	1.886	0.0092	0.712	23.326	0.805	0.188	28	2000	1400000	**136.53**	25.82
BH02 - 09	3816.114	2.270	1698165.218	1.290	0.0022	1.240	5.535	1.296	0.072	16	3000	533333.3	**217.79**	54.52

BH02 - 11	19240.622	1.161	1663389.973	0.764	0.0115	0.606	29.425	0.716	0.211	40	1500	2666667	**205.05**	32.45
BH02 - 12	13348.020	1.500	1399682.421	1.187	0.0095	0.667	24.175	0.769	0.186	24	1200	2000000	**187.44**	38.29
BH02 - 13	3981.588	2.830	1238034.769	2.423	0.0032	1.032	8.166	1.108	0.090	10	2000	500000	**139.25**	44.06
BH02 - 14	17026.330	1.212	1470974.156	0.944	0.0117	1.304	29.408	1.365	0.402	17	1600	1062500	**82.53**	20.05
BH02 - 15	7311.183	1.698	829580.714	1.636	0.0088	0.619	22.178	0.742	0.165	21	1400	1500000	**153.65**	33.55
BH02 - 16	4214.937	1.084	1683936.969	0.643	0.0025	0.860	6.289	0.953	0.060	15	2500	600000	**215.69**	55.73
BH02 - 17	16632.097	1.267	1861408.786	1.266	0.0089	1.235	22.319	1.303	0.291	27	2100	1285714	**131.10**	25.29
BH02 - 18	2981.969	1.152	1464283.179	0.796	0.0020	1.241	5.211	1.309	0.068	12	2400	500000	**216.91**	62.68
BH02 - 19	18226.590	0.985	1622498.180	0.947	0.0112	0.591	28.718	0.724	0.208	22	2000	1100000	**87.46**	18.66
BH02 - 20	17188.589	1.014	1689926.578	0.985	0.0102	0.382	25.257	0.568	0.144	29	2500	1160000	**104.73**	19.46
BH03 - 2	31563.308	0.704	1697122.409	0.617	0.0186	0.660	46.121	0.805	0.371	38	1600	2375000	**116.79**	18.97
BH03 - 3	24299.597	0.797	1778463.198	0.956	0.0137	0.545	34.301	0.715	0.245	37	2000	1850000	**122.27**	20.12
BH03 - 4	17698.169	0.736	1794179.373	0.491	0.0099	0.927	24.118	1.038	0.250	38	2500	1520000	**142.65**	23.19
BH03 - 5	21981.659	0.765	1821963.072	0.599	0.0121	0.951	30.273	1.060	0.321	24	2100	1142857	**85.83**	17.54
BH03 - 6	35412.322	1.086	1664993.379	0.831	0.0212	0.481	53.220	0.673	0.358	58	2000	2900000	**123.52**	16.24
BH03 - 7	15061.920	0.735	1739161.572	0.472	0.0087	0.714	21.592	0.857	0.185	60	5000	1200000	**125.96**	16.30
BH03 - 10	10409.423	1.865	1624476.575	1.425	0.0064	0.685	15.693	0.847	0.133	19	3500	542857.1	**78.68**	18.06
BH03 - 11	29737.867	0.510	1751774.496	0.656	0.0170	0.777	41.778	0.924	0.386	70	4000	1750000	**95.16**	11.41
BH03 - 13	11612.436	0.675	1772317.405	0.532	0.0066	0.881	16.359	1.016	0.166	48	7000	685714.3	**95.23**	13.78
BH03 - 14	14904.372	2.651	626612.965	3.087	0.0240	1.033	58.926	1.151	0.678	48	1600	3000000	**115.48**	16.72
BH03 - 16	19422.542	0.657	1576956.930	0.609	0.0123	0.490	30.394	0.724	0.220	47	3500	1342857	**100.33**	14.65
BH03 - 21	15680.225	0.664	1601558.539	0.818	0.0098	0.577	24.261	0.793	0.192	30	2500	1200000	**112.22**	20.51
BH03 - 22	35152.778	0.969	1595871.802	0.801	0.0220	0.380	54.841	0.666	0.365	67	2500	2680000	**110.88**	13.57
BH03 - 23	36497.624	0.676	1752442.973	0.553	0.0208	0.679	51.328	0.874	0.449	60	2500	2400000	**106.13**	13.73
BH04 - 1	12018.552	0.977	1741605.804	0.491	0.0069	0.857	17.125	0.929	0.159	29	2100	1380952	**181.96**	33.83
BH04 - 2	6627.718	1.181	1708413.109	0.851	0.0039	0.858	9.649	0.930	0.090	53	10000	530000	**124.50**	17.14
BH04 - 3	14979.863	0.497	1735555.680	0.657	0.0086	0.589	21.509	0.691	0.149	31	2800	1107143	**116.74**	20.98
BH04 - 4	2345.924	1.649	1667796.507	0.661	0.0014	1.533	3.500	1.575	0.055	13	4900	265306.1	**171.20**	47.56

BH04 - 6	13625.931	1.518	1578626.338	0.732	0.0086	0.892	21.454	0.964	0.207	29	3000	966666.7	**102.30**	19.02
BH04 - 7	6600.705	1.785	1796272.003	0.765	0.0037	1.230	9.179	1.284	0.118	39	5600	696428.6	**171.35**	27.53
BH04 - 9	10346.805	0.772	1730027.889	0.424	0.0060	0.712	14.852	0.811	0.120	31	5000	620000	**94.84**	17.05
BH04 - 10	7252.337	1.533	1662909.991	0.551	0.0044	1.406	10.932	1.459	0.160	32	4200	761904.8	**157.56**	27.95
BH04 - 11	2335.342	1.352	1634390.468	0.984	0.0014	1.209	3.555	1.271	0.045	18	4200	428571.4	**270.16**	63.77
BH04 - 14	5682.223	0.937	1838213.186	0.550	0.0031	0.787	7.670	0.882	0.068	19	6400	296875	**87.98**	20.20
BH04 - 15	13497.274	0.913	1817515.311	0.717	0.0074	0.836	18.429	0.927	0.171	30	4000	750000	**92.47**	16.91
BH04 - 16	15164.110	1.218	1523198.220	0.826	0.0100	1.132	24.846	1.201	0.298	16	2500	640000	**58.68**	14.69
BH04 - 18	4592.099	1.005	1732717.150	0.780	0.0027	0.999	6.530	1.085	0.071	13	3500	371428.6	**128.89**	35.77
BH04 - 19	9945.548	0.909	1814901.341	0.577	0.0055	0.901	13.626	0.996	0.136	18	4200	428571.4	**71.59**	16.89
BH04 - 20	3376.269	0.853	1518608.712	0.712	0.0022	0.792	5.530	0.900	0.050	20	6000	333333.3	**136.49**	30.54
BH04 - 21	5073.480	1.116	1648863.850	0.752	0.0031	0.800	7.675	0.908	0.070	40	7000	571428.6	**168.18**	26.63
BH04 - 22	3408.167	1.044	1731794.808	0.783	0.0020	1.207	4.914	1.282	0.063	40	10000	400000	**183.64**	29.13
BH04 - 23	12590.127	1.273	1815901.993	0.552	0.0069	1.088	17.300	1.171	0.203	17	2500	680000	**89.34**	21.69
BH04 - 25	8135.963	1.262	1642144.816	1.086	0.0050	0.628	12.415	0.777	0.096	15	2500	600000	**109.67**	28.33
BH05 - 2	3948.817	1.217	1831183.722	0.693	0.0022	0.952	5.487	1.005	0.055	9	2500	360000	**163.96**	54.68
BH05 - 3	23643.047	1.077	1862681.484	0.723	0.0127	0.636	32.387	0.713	0.231	175	10000	1750000	**135.35**	10.28
BH05 - 4	12666.389	1.656	2044820.223	1.026	0.0062	0.842	15.722	0.909	0.143	61	6400	953125	**151.66**	19.47
BH05 - 6	6404.243	1.118	2074819.128	1.279	0.0031	1.345	7.914	1.389	0.110	16	2000	800000	**250.93**	62.83
BH05 - 8	12257.602	1.330	2277029.057	0.973	0.0054	1.152	13.692	1.204	0.165	12	1200	1000000	**182.27**	52.66
BH05 - 10	12445.106	1.211	2220924.164	0.682	0.0056	1.294	14.313	1.342	0.192	22	2000	1100000	**191.66**	40.94
BH05 - 15	5006.164	1.600	1900566.627	1.280	0.0026	1.074	6.714	1.139	0.076	19	5000	380000	**141.70**	32.55
BH05 - 17	6176.296	1.395	1714278.313	0.417	0.0036	1.296	9.090	1.352	0.123	11	2500	440000	**121.38**	36.63
BH05 - 18	4225.448	0.852	1878825.302	0.846	0.0023	1.183	5.732	1.244	0.071	12	2400	500000	**217.09**	62.73
BH06 - 2	18831.274	1.211	1744595.026	0.734	0.0108	0.856	27.506	0.887	0.244	31	2500	1240000	**113.11**	20.34
BH06 - 4	14120.408	1.161	1767483.291	0.806	0.0080	0.888	20.235	0.923	0.187	24	2500	960000	**118.99**	24.31
BH06 - 5	13614.944	1.849	1810061.053	1.167	0.0075	0.918	19.258	0.952	0.183	50	2500	2000000	**257.66**	36.52
BH06 - 6	17653.608	0.984	1731181.824	0.872	0.0102	0.405	25.888	0.478	0.124	41	2500	1640000	**158.39**	24.75

BH06 - 7	12346.540	0.983	1950390.328	0.649	0.0064	1.394	15.984	1.417	0.227	19	2500	760000	**119.25**	27.41
BH06 - 8	8456.815	2.106	1871220.403	0.729	0.0046	2.692	11.490	2.704	0.311	26	2500	1040000	**225.14**	44.57
BH06 - 9	4460.504	1.026	1768336.311	0.760	0.0025	0.653	6.363	0.703	0.045	20	3000	666666.7	**259.90**	58.14
BH06 - 10	4447.247	2.128	958540.185	1.471	0.0046	1.060	11.741	1.092	0.128	22	2500	880000	**186.99**	39.92
BH06 - 11	17783.314	1.006	1586510.760	0.620	0.0112	0.715	28.159	0.767	0.216	23	2000	1150000	**102.56**	21.40
BH06 - 12	16351.849	0.866	1708358.874	0.763	0.0096	0.456	24.427	0.536	0.131	37	2500	1480000	**151.57**	24.93
BH06 - 13	21128.399	0.666	1903455.230	0.639	0.0111	0.958	27.816	0.998	0.278	33	2000	1650000	**148.43**	25.88
BH06 - 14	16757.559	1.016	1826742.504	1.094	0.0092	0.576	23.343	0.642	0.150	41	2500	1640000	**175.43**	27.42
BH06 - 16	11580.576	1.297	1481032.356	0.540	0.0078	0.976	19.885	1.018	0.202	18	2000	900000	**113.56**	26.79
BH06 - 18	20279.343	0.545	1801170.486	0.769	0.0113	0.651	28.014	0.714	0.200	25	2500	1000000	**89.73**	17.96
BH06 - 19	13763.273	0.774	1752348.927	0.789	0.0079	0.492	19.949	0.582	0.116	28	2500	1120000	**140.57**	26.58
BH06 - 20	17446.769	0.697	1729654.995	0.827	0.0101	0.736	25.673	0.799	0.205	26	2500	1040000	**101.73**	19.97
BH06 - 21	10370.116	0.982	1727064.142	0.798	0.0060	0.560	15.374	0.642	0.099	56	8000	700000	**114.24**	15.28
BH06 - 22	15754.481	1.181	1838061.380	0.548	0.0086	0.917	21.859	0.970	0.212	27	2500	1080000	**123.87**	23.87
BH06 - 23	18119.106	1.198	1850001.861	0.679	0.0098	0.700	25.009	0.769	0.192	56	5000	1120000	**112.37**	15.04
BH07 - 1	23829.752	0.908	1680252.690	0.900	0.0142	0.369	35.926	0.468	0.168	154	8000	1925000	**121.48**	9.81
BH07 - 2	16113.750	0.772	1928598.385	0.647	0.0084	0.773	21.158	0.825	0.175	61	4000	1525000	**162.88**	20.90
BH07 - 3	28568.329	0.796	1711603.585	0.662	0.0167	0.348	42.193	0.452	0.191	192	9000	2133333	**114.69**	8.29
BH07 - 4	12492.240	1.362	1771787.177	0.814	0.0070	0.651	17.858	0.712	0.127	87	7200	1208333	**153.02**	16.44
BH07 - 5	17967.096	0.881	1698980.621	0.620	0.0106	0.491	26.806	0.570	0.153	103	6400	1609375	**135.96**	13.42
BH07 - 6	11221.084	0.765	1680134.812	0.766	0.0067	0.466	17.043	0.549	0.094	139	10000	1390000	**184.01**	15.64
BH07 - 7	6764.970	1.250	1812704.919	0.804	0.0037	1.104	9.437	1.141	0.108	53	6000	883333.3	**210.74**	29.05
BH07 - 8	6117.369	1.126	1728984.421	0.760	0.0035	0.685	8.940	0.744	0.067	68	7000	971428.6	**244.02**	29.65
BH07 - 9	10589.963	1.661	1732488.539	0.837	0.0061	0.966	15.471	1.010	0.156	87	7000	1242857	**181.29**	19.52
BH07 - 10	9095.586	0.856	1702411.364	0.986	0.0054	0.564	13.543	0.637	0.086	63	4800	1312500	**218.07**	27.51
BH07 - 11	9534.834	0.846	1926602.061	0.467	0.0050	0.837	12.570	0.888	0.112	46	5400	851851.9	**153.26**	22.64
BH07 - 12	7987.422	1.082	1711257.290	0.796	0.0047	0.551	11.853	0.627	0.074	34	4900	693877.6	**132.60**	22.76
BH07 - 13	8812.052	1.137	1729904.682	0.512	0.0051	1.232	12.992	1.267	0.165	105	10000	1050000	**182.36**	17.95

BH07 - 14	10088.735	0.683	1850542.368	0.583	0.0055	0.817	13.900	0.870	0.121	69	5000	1380000	**223.31**	26.95
BH07 - 15	11097.387	1.323	1346260.172	1.009	0.0082	0.959	20.905	1.005	0.210	80	5000	1600000	**172.83**	19.40
BH08 - 1	35262.532	1.221	1600344.077	0.909	0.0220	0.815	55.712	0.869	0.484	53	3000	1766667	**72.17**	9.93
BH08 - 2	17937.916	1.335	1790674.841	0.510	0.0100	1.117	24.956	1.159	0.289	33	2800	1178571	**107.19**	18.70
BH08 - 3	24489.636	0.807	1569963.763	0.809	0.0156	0.354	39.417	0.471	0.186	60	4500	1333333	**76.95**	9.94
BH08 - 4	27168.545	0.817	1541892.986	0.637	0.0176	0.446	43.925	0.545	0.239	75	5400	1388889	**71.96**	8.32
BH08 - 6	16381.008	0.565	1641732.086	0.762	0.0100	0.558	25.055	0.641	0.160	86	8100	1061728	**96.26**	10.40
BH08 - 7	7698.090	0.877	1652451.140	1.083	0.0047	0.851	11.751	0.908	0.107	81	8000	1012500	**194.24**	21.65
BH08 - 8	9342.174	1.013	1651996.575	0.809	0.0057	0.642	14.258	0.717	0.102	14	2000	700000	**111.39**	29.78
BH08 - 10	12590.598	1.267	1557370.888	0.760	0.0081	0.650	20.312	0.730	0.148	67	6300	1063492	**118.73**	14.53
BH08 - 11	27307.448	2.121	1769705.532	0.566	0.0154	1.717	38.677	1.749	0.677	96	5000	1920000	**112.62**	11.66
BH08 - 12	10236.543	0.855	1797552.232	0.513	0.0057	1.084	14.304	1.134	0.162	40	5000	800000	**126.75**	20.09
BH08 - 13	22087.437	0.791	1563195.897	0.770	0.0142	0.642	35.681	0.725	0.259	79	5000	1580000	**100.56**	11.34
BH08 - 14	11996.333	0.922	1691762.829	0.776	0.0071	0.904	17.774	0.965	0.171	46	4900	938775.5	**119.76**	17.70
BH08 - 15	21866.137	0.813	1522145.204	0.725	0.0144	0.359	36.198	0.494	0.179	93	6400	1453125	**91.23**	9.47
BH08 - 16	21543.077	0.921	1681262.568	0.619	0.0128	0.560	32.195	0.656	0.211	99	4200	2357143	**165.42**	16.66
BH08 - 17	6562.039	0.639	1668934.307	0.845	0.0039	0.838	9.990	0.905	0.090	25	4800	520833.3	**118.23**	23.67
BH09 - 01	11919.586	1.844	1914089.701	1.455	0.0062	0.700	15.353	0.829	0.127	24	4900	489795.9	**72.93**	14.90
BH09 - 02	9947.368	1.148	1815183.066	1.258	0.0055	0.548	13.782	0.707	0.097	58	7000	828571.4	**136.75**	17.98
BH09 - 03	9812.381	1.288	1714465.939	1.272	0.0057	0.444	14.491	0.631	0.091	55	6400	859375	**134.92**	18.21
BH09 - 04	17674.971	1.147	1703444.261	1.097	0.0104	0.536	26.357	0.701	0.185	81	6400	1265625	**109.46**	12.19
BH09 - 05	11372.388	1.472	1894772.529	0.773	0.0060	1.227	15.343	1.309	0.201	20	2500	800000	**118.77**	26.60
BH09 - 06	7879.493	1.291	1957870.380	0.816	0.0040	0.921	10.270	1.029	0.106	29	4000	725000	**160.28**	29.81
BH09 - 07	12813.551	0.918	1764881.901	1.054	0.0073	0.493	18.513	0.674	0.125	51	4800	1062500	**130.61**	18.31
BH09 - 08	11445.872	0.950	1774204.219	1.037	0.0065	0.495	16.519	0.677	0.112	50	6000	833333.3	**114.94**	16.27
BH09 - 09	12518.059	1.150	1659241.061	1.114	0.0075	0.444	19.093	0.659	0.126	51	3600	1416667	**168.36**	23.60
BH09 - 10	8522.865	1.191	1760882.392	1.077	0.0048	0.698	12.326	0.853	0.105	45	6400	703125	**129.83**	19.39
BH09 - 11	8531.952	0.966	1880733.067	0.759	0.0045	0.516	11.554	0.714	0.082	118	10000	1180000	**230.61**	21.29

BH09 - 12	10135.752	1.013	1877615.360	0.618	0.0054	0.578	13.715	0.762	0.104	29	3600	805555.6	**133.63**	24.84
BH09 - 13	13310.239	0.486	1690631.599	0.658	0.0079	0.692	20.253	0.853	0.173	77	7000	1100000	**123.67**	14.13
BH09 - 14	14820.419	1.264	1927906.236	1.121	0.0077	0.599	19.624	0.781	0.153	30	2500	1200000	**139.07**	25.41
BH09 - 15	10370.049	0.832	1666759.064	0.653	0.0062	0.504	15.916	0.713	0.113	73	4900	1489796	**211.69**	24.82
BH09 - 16	10329.632	1.063	1847614.948	0.766	0.0056	0.605	14.277	0.790	0.113	30	2500	1200000	**190.39**	34.79
BH09 - 17	14136.475	1.082	1652651.072	0.822	0.0085	0.456	21.853	0.702	0.153	33	3500	942857.1	**98.44**	17.15
BH09 - 18	8755.085	0.551	1845088.891	0.635	0.0048	0.685	12.196	0.871	0.106	26	2500	1040000	**193.13**	37.91
BH09 - 20	17101.337	1.545	1741035.053	1.236	0.0098	0.512	25.035	0.746	0.187	41	3000	1366667	**124.30**	19.43
BH10 - 02	3936.894	1.229	1651925.221	1.202	0.0024	0.679	6.066	0.873	0.053	12	2800	428571.4	**160.42**	46.33
BH10 - 03	5358.958	1.549	1569483.928	0.806	0.0034	1.183	8.891	1.305	0.116	11	1500	733333.3	**186.88**	56.40
BH10 - 04	4827.226	1.305	1772769.200	1.187	0.0027	1.093	6.964	1.226	0.085	24	3000	800000	**258.82**	52.93
BH10 - 06	6352.308	1.675	1852228.772	1.575	0.0034	1.073	8.771	1.223	0.107	30	5000	600000	**155.38**	28.43
BH10 - 07	7004.511	1.576	1648555.975	1.233	0.0042	0.617	10.748	0.853	0.092	4	1200	333333.3	**70.91**	35.46
BH10 - 10	11214.147	1.414	1685253.118	1.060	0.0066	0.785	16.914	0.987	0.167	21	2400	875000	**117.85**	25.74
BH10 - 15	6987.095	1.589	1813517.229	0.932	0.0039	1.127	9.795	1.295	0.127	15	3200	468750	**109.10**	28.20
BH10 - 16	7153.081	1.535	1597902.036	1.309	0.0045	0.603	11.335	0.881	0.100	21	2800	750000	**150.35**	32.84
BH10 - 17	12532.060	1.935	1708942.457	1.251	0.0073	0.902	18.627	1.109	0.207	27	3000	900000	**110.13**	21.23
BH10 - 18	10352.268	1.465	2005349.597	0.915	0.0052	0.791	13.134	1.023	0.134	14	1500	933333.3	**161.34**	43.15
BH10 - 20	8512.884	1.306	1873604.911	0.706	0.0045	1.168	11.690	1.339	0.157	20	2100	952381	**184.63**	41.36
BH12 - 1	9599.777	1.295	1919050.981	0.842	0.0050	1.083	11.749	1.538	0.181	36	7000	514285.7	**101.53**	16.99
BH12 - 2	9174.948	0.587	1943961.224	0.591	0.0047	0.537	10.999	1.226	0.135	13	3000	433333.3	**91.45**	25.39
BH12 - 3	18006.747	0.994	1918803.003	0.674	0.0094	0.800	22.096	1.370	0.303	48	6000	800000	**84.09**	12.19
BH12 - 4	9582.598	0.813	1806416.784	0.684	0.0053	0.694	12.285	1.319	0.162	25	4900	510204.1	**96.37**	19.32
BH12 - 6	12013.733	1.048	2058832.445	0.438	0.0058	0.950	13.617	1.549	0.211	28	2500	1120000	**189.48**	35.93
BH12 - 7	18745.822	0.957	1885708.051	0.648	0.0099	0.521	22.705	1.340	0.304	90	7000	1285714	**131.04**	13.92
BH12 - 8	12383.178	0.708	1882968.514	0.580	0.0066	0.429	14.971	1.316	0.197	26	3500	742857.1	**114.97**	22.60
BH12 - 10	11217.781	0.962	2004091.442	0.859	0.0056	0.477	12.948	1.353	0.175	18	2400	750000	**134.02**	31.64
BH12 - 11	16935.159	0.723	2054339.690	0.415	0.0082	0.752	19.272	1.481	0.285	21	3500	600000	**72.38**	15.83

BH12 - 14	42937.026	1.025	1941017.010	0.676	0.0221	0.498	49.501	1.483	0.734	111	4800	2312500	**108.30**	10.40
BH12 - 15	5881.327	0.853	1853367.756	0.711	0.0032	0.568	7.322	1.518	0.111	11	7000	157142.9	**49.98**	15.09
BH12 - 16	5349.989	1.230	1878302.247	0.648	0.0028	0.799	6.556	1.628	0.107	27	3500	771428.6	**269.40**	52.03
BH12 - 17	28268.843	0.668	1939020.213	0.637	0.0146	0.425	33.599	1.491	0.501	111	7000	1585714	**109.40**	10.51
BH12 - 18	1915.600	1.402	1885862.684	0.645	0.0010	1.195	2.308	1.872	0.043	12	10000	120000	**120.45**	34.84
BH12 - 19	8884.862	0.605	2019006.901	0.512	0.0044	0.685	10.110	1.606	0.162	45	6400	703125	**160.57**	24.08
BH12 - 20	6776.787	1.037	2050498.267	0.690	0.0033	0.814	7.463	1.675	0.125	17	4000	425000	**131.77**	32.04
BH12 - 22	12427.261	0.702	1861297.549	0.614	0.0067	0.421	15.331	1.632	0.250	63	8000	787500	**118.98**	15.12
BH12 - 24	26907.341	0.757	1940149.277	0.734	0.0139	0.341	32.211	1.636	0.527	90	8000	1125000	**81.14**	8.66
BH12 - 25	17343.056	0.662	1985785.855	0.626	0.0088	0.876	20.184	1.834	0.370	54	5400	1000000	**114.80**	15.76
BH12 - 26	20798.813	0.701	1878715.082	0.417	0.0111	0.575	24.977	1.722	0.430	83	6300	1317460	**122.15**	13.57
BH13 - 3	15564.121	0.881	2078573.059	0.863	0.0075	0.844	19.219	0.857	0.165	77	4000	1925000	**248.68**	28.42
BH13 - 4	16831.661	0.824	2044888.825	0.772	0.0082	0.562	20.991	0.582	0.122	24	2000	1200000	**143.11**	29.22
BH13 - 5	15012.243	0.705	2096269.830	0.511	0.0072	0.714	18.270	0.730	0.133	18	2000	900000	**123.50**	29.12
BH13 - 6	10823.850	1.235	1964992.732	0.552	0.0055	0.936	14.131	0.949	0.134	25	2700	925925.9	**163.76**	32.79
BH13 - 7	27475.749	0.584	2087210.100	0.656	0.0132	0.480	33.927	0.503	0.171	65	4200	1547619	**114.45**	14.21
BH13 - 8	43419.094	0.591	2176757.183	0.499	0.0200	0.502	51.360	0.525	0.269	109	4000	2725000	**132.92**	12.75
BH13 - 9	19263.188	0.627	2019204.474	0.610	0.0095	0.513	24.491	0.537	0.131	47	3000	1566667	**159.92**	23.34
BH13 - 11	28743.861	1.054	2122628.726	0.567	0.0135	0.675	34.738	0.694	0.241	189	10000	1890000	**136.27**	9.96
BH13 - 12	16980.303	0.604	1915968.106	0.412	0.0089	0.406	22.371	0.436	0.098	33	2500	1320000	**147.65**	25.71
BH13 - 13	33125.687	0.683	2125246.117	0.572	0.0156	0.720	40.296	0.738	0.297	55	4900	1122449	**70.13**	9.47
BH13 - 14	7258.354	2.054	1960845.985	0.600	0.0037	1.580	9.365	1.588	0.149	53	5600	946428.6	**250.87**	34.69
BH13 - 15	8382.589	1.041	2036254.820	0.578	0.0041	1.113	10.505	1.125	0.118	12	4200	285714.3	**68.48**	19.78
BH13 - 16	18988.576	0.888	1911228.517	0.845	0.0100	0.652	25.411	0.672	0.171	32	3000	1066667	**105.39**	18.64
BH13 - 17	9277.420	1.886	1885951.815	1.379	0.0049	1.051	12.495	1.066	0.133	23	2500	920000	**183.73**	38.36
BH13 - 18	12517.186	1.501	2017651.576	0.597	0.0062	1.320	15.843	1.332	0.211	43	4000	1075000	**169.51**	25.95
BH14 - 1	13608.761	0.987	1904472.976	0.604	0.0071	0.597	18.122	0.623	0.113	27	2500	1080000	**149.12**	28.71
BH14 - 2	7757.849	0.802	1925347.873	0.608	0.0040	0.716	10.149	0.738	0.075	24	2500	960000	**235.10**	48.02

BH14 - 3	13004.765	1.191	1989909.793	0.531	0.0065	0.947	16.704	0.964	0.161	32	2500	1280000	**191.10**	33.83
BH14 - 4	18822.037	0.660	1858809.295	0.713	0.0101	0.454	25.857	0.489	0.126	46	4500	1022222	**99.30**	14.65
BH14 - 5	20671.063	1.179	1530267.198	1.296	0.0136	0.481	34.633	0.515	0.178	50	5000	1000000	**72.68**	10.28
BH14 - 6	14126.237	1.195	2030460.235	0.901	0.0070	1.057	17.724	1.072	0.190	35	4000	875000	**123.77**	20.96
BH14 - 7	15922.353	0.938	2002201.771	0.601	0.0079	0.583	20.166	0.615	0.124	41	3500	1171429	**145.38**	22.72
BH14 - 8	24587.991	0.711	2005374.084	0.575	0.0123	0.717	30.434	0.743	0.226	38	2500	1520000	**125.20**	20.33
BH14 - 10	20232.362	0.551	1844011.258	0.783	0.0110	0.495	27.908	0.534	0.149	26	2000	1300000	**116.85**	22.92
BH14 - 11	36444.453	0.738	1973613.397	0.777	0.0185	0.723	46.382	0.751	0.348	45	2000	2250000	**121.64**	18.16
BH14 - 12	20530.117	0.562	1991963.989	0.749	0.0103	0.660	26.188	0.691	0.181	53	2500	2120000	**201.73**	27.74
BH14 - 13	13093.145	2.510	1555231.326	2.079	0.0084	0.761	21.221	0.788	0.167	29	3200	906250	**107.20**	19.93
BH14 - 14	18039.501	1.478	1709989.461	1.408	0.0106	0.507	26.837	0.548	0.147	80	6000	1333333	**124.55**	13.94
BH14 - 15	11052.811	2.552	1805190.028	1.610	0.0061	1.352	15.242	1.370	0.209	29	3500	828571.4	**136.15**	25.35
BH14 - 16	16248.060	1.654	1867502.708	0.704	0.0087	1.032	21.663	1.056	0.229	18	1600	1125000	**130.13**	30.70
BH14 - 17	14052.682	0.667	1800139.806	0.772	0.0078	0.493	19.868	0.542	0.108	66	3500	1885714	**235.88**	29.06
BH14 - 18	11084.055	0.982	1784438.306	0.899	0.0062	0.617	15.612	0.658	0.103	46	3500	1314286	**209.64**	30.94
BH14 - 19	18815.071	1.784	1942491.614	0.858	0.0097	1.017	24.872	1.042	0.259	37	2500	1480000	**148.89**	24.53
BH14 - 20	8787.538	0.656	1927920.172	0.607	0.0046	0.846	11.576	0.877	0.101	32	6000	533333.3	**115.58**	20.46
BH15 - 1	57573.779	1.100	1883040.940	1.329	0.0306	0.487	73.211	0.972	0.712	169	4900	3448980	**109.21**	8.47
BH15 - 2	68048.068	2.163	1837232.142	1.357	0.0368	0.970	87.718	1.288	1.130	88	2500	3520000	**93.14**	10.00
BH15 - 3	72341.957	1.146	1675367.290	1.108	0.0432	0.270	103.226	0.895	0.924	454	10000	4540000	**102.01**	4.87
BH15 - 4	67504.574	0.917	1615952.009	0.928	0.0419	0.557	99.797	1.073	1.071	91	2500	3640000	**84.71**	8.93
BH15 - 5	100507.138	1.572	1668908.752	1.271	0.0600	0.407	141.106	1.011	1.426	167	2500	6680000	**109.74**	8.56
BH15 - 6	76792.410	0.564	1650504.352	0.611	0.0466	0.305	110.915	0.982	1.089	129	2500	5160000	**107.86**	9.56
BH15 - 7	48868.237	0.663	1653765.556	0.782	0.0296	0.310	69.568	0.991	0.689	78	2500	3120000	**104.01**	11.82
BH15 - 8	57899.617	1.115	1703077.657	1.287	0.0341	0.437	80.951	1.045	0.846	102	2500	4080000	**116.77**	11.63
BH15 - 9	79156.710	1.083	1636783.412	0.867	0.0483	0.327	113.093	1.011	1.144	127	2500	5080000	**104.17**	9.30
BH15 - 10	61083.185	0.788	1638436.519	0.759	0.0373	0.275	88.296	1.004	0.886	88	2500	3520000	**92.53**	9.91
BH15 - 11	78284.370	1.234	1623574.640	1.171	0.0482	0.276	113.312	1.013	1.147	110	2500	4400000	**90.15**	8.64

BH15 - 12	82524.646	0.682	1763406.674	1.080	0.0470	0.896	111.100	1.384	1.537	124	2500	4960000	**103.54**	9.41
BH15 - 13	59766.644	1.053	1757203.902	0.711	0.0340	0.519	79.514	1.184	0.941	85	2500	3400000	**99.20**	10.82
BH15 - 14	46064.380	0.762	1603318.034	0.557	0.0287	0.364	67.443	1.133	0.764	90	2500	3600000	**123.60**	13.10
BH15 - 15	68377.372	1.483	1631655.474	1.146	0.0418	0.482	98.441	1.185	1.167	108	2500	4320000	**101.79**	9.87
BH16 - 1	9485.961	1.067	1511117.302	0.819	0.0063	1.417	15.000	1.610	0.242	10	1500	666666.7	**103.08**	32.64
BH16 - 3	35030.166	0.541	1808980.187	0.453	0.0194	0.632	46.843	0.993	0.465	92	3500	2628571	**129.87**	13.60
BH16 - 4	57737.978	0.549	1731251.167	0.731	0.0334	0.562	79.754	0.952	0.759	54	2400	2250000	**65.62**	8.95
BH16 - 5	6311.124	0.702	1791919.450	0.594	0.0035	0.812	8.582	1.119	0.096	10	2000	500000	**134.79**	42.65
BH16 - 8	21965.397	2.715	1774177.654	1.928	0.0123	1.240	29.736	1.463	0.435	30	1800	1666667	**129.72**	23.76
BH16 - 12	44935.043	4.815	1861883.044	3.170	0.0237	2.129	55.769	2.285	1.274	62	2000	3100000	**128.66**	16.60

APPENDIX B: EXTENDED METHOD

Crushing and separation

Crushing and separation of the samples was performed at the Institute of Geology and Geophysics, Chinese Academy of Sciences using conventional procedures.

Picking

The first step of the AFT analysis process involved the picking of appropriate apatite grains under a low magnification (~45X) picking microscope. Two Olympus SZ61 picking microscopes were placed side by side. Shallow dishes of ~10cm diameter were thoroughly cleaned with ethanol and placed under each microscope. The apatite fraction of the separate for one sample was partially poured into the dish under one microscope, while a microscope slide with a square of double-sided tape was placed under the other. The square of tape was placed as in Fig. 1 in order to allow for the maximum density of samples per slide while still allowing the slide to be placed within the laser chamber of the Resonetics M-50 laser ablation system in a later stage of analysis.

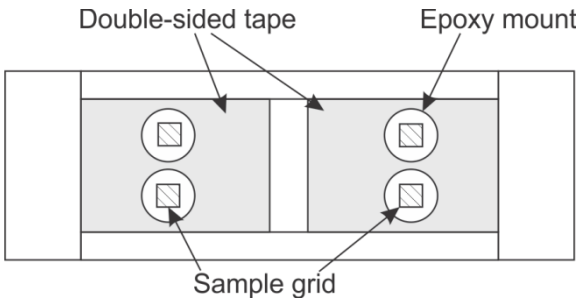

Figure 1. Configuration of slide for picking and mounting

Apatite crystals have a characteristic stubby hexagonal crystal shape and a clear colour. Crystals for analysis were chosen on the basis of good crystal shape, clarity and a lack of obvious inclusions or fractures. The grain size distribution of the picked grains mimicked the distribution of the grains in the sample, while avoiding crystals <~50μm which may be lost during laser ablation. Grains were picked from the matrix using a

fine needle and were arranged on the double sided tape in a grid typically 10x10 to 15x15 in size. In total 100-225 grains were selected per sample depending on the size, quality and quantity of apatite grains.

Mounting

A 5:1 mixture of epoxy resin to epoxy hardener was prepared to embed the apatite separates. A small plastic cup was placed on a set of scales which were then zeroed. 1g of resin was poured carefully into the cup, followed by 0.2g of hardener. The mixture was stirred until it became clear and homogeneous, with great care being taken not to introduce air bubbles by vigorous or careless stirring. The mixture was dripped one drop at a time with a toothpick onto the sample grid until all grains were entirely covered, and then a cleaned slide was placed precisely on top of the picking slide. Extra slides were used as spacers between the mount slide and the picking slide to ensure the epoxy mount was exactly one slide in thickness. The mounts were left to dry for 3 days to a week. Once dried, a razor blade was used to separate the sticky tape from the picking slide. The tape was then peeled off the mount to expose the apatite crystals for further treatment.

Grinding

Fine sandpaper was used to remove the sticky tape residue and to expose an internal section of the apatite crystals. 1000 grain sandpaper was splashed with a few millilitres of water and the slide was rubbed against it in a figure-eight pattern. Frequent checks under a picking microscope were used to gauge the degree of grinding. As the degree of grinding approached the desired level, finer grained sandpaper were employed to avoid overgrinding and to smoothen the grains prior to polishing. The initial texture of the mount surface was vitreous, uneven and slightly reflective. After an appropriate degree

of grinding was accomplished, the surface became more even and less reflective, with small regular scratches covering the surface evenly. Once the sample grid was ground to this stage, an internal section of the apatite grains was exposed. Care was taken to only remove the top 1/3-1/4 of the apatite so as that a rim of epoxy was still in place to hold the crystal in the mount during laser ablation.

Polishing

The edges and corners of the slide were ground down on a disc grinder prior to polishing in order to prevent damage to the polishing cloths.

Two polishing cloths were used in order to achieve a smooth mount surface. It is essential to ensure that the correct diamond suspension paste was used with each cloth otherwise their effectiveness would be greatly diminished. The 3μm cloth and paste were used first to remove large imperfections and scratches. A few small squirts of paste were applied to the cloth, and the speed of the polisher was set to 1.5 on the bottom of the dial using the small knob on the left hand side of the control panel. The slide was placed into a small bronze holder and fastened in using the appropriate Alan key. This was placed 1/3 of the way out from the centre of the spinning cloth and held in place gently, with the majority of the downwards force provided by the weight of the bronze holder. The slider and holder were slowly rotated in order to evenly polish the mount. The mount was polished in five minute intervals for a total of around 15 minutes. The mount was checked between polishing sessions under a high powered (>100X magnification) microscope. Polishing continued until no further improvement of the surface was apparent. The 1um cloth was then used in the same fashion to polish the surface further, usually for 1-2 five minute intervals.

Etching

Chemical etching is required to reveal the fission tracks. The samples were cleaned with alcohol and dried to avoid contamination or dilution of the etching solution. A beaker approximately 4cm in diameter and 6cm high was half filled with 5M HNO_3 at 20^0C and a large (~1L) beaker was filled with deionised water. The size of the small beaker and the level of HNO_3 were sufficient for two mounts on a single slide to be entirely submerged. The mounts were submerged in the HNO_3 for 20 seconds and were then placed into the beaker of water to rapidly dilute the acid and prevent further etching.

Counting

The etched mounts were then placed under an Olympus BX51 high powered (1000X magnification) microscope with attached camera system for counting track density and measuring confined track lengths. One of the eyepieces of the microscope contains a 100x100μm grid that is used to define the area which will be counted. This grid is placed over a suitable apatite grain and the size of the counted area is noted. Suitable apatite grains have uniform track density, no inclusions or fractures and have an even surface to facilitate fast and accurate counting. Fission tracks can be seen as 8-16μm linear features in the crystal that have a small 'etch pit' where the track intersects the surface (Fig. 2). All the fission tracks in the nominated area are counted, with the position of the pit on the surface determining whether tracks fall into the counted area. In the case of a pit which falls exactly on the edge of the grid, a systematic approach is used to count half of them; those pits that fall on the very edge of the 'top' and 'left' of the grid are counted and those that fall on the 'right' and 'bottom' of the grid area not. The location of the counted area on each grain was added to a photographic map of the

mount so that determination of the concentration of U could accurately be carried out on the same area.

In addition to an apatite fission track age determination based on the counted fission track densities, an estimation of the cooling rate was carried our using so-called 'confined fission track' measurements. Confined fission tracks are those tracks that are intersected by another track or by a fracture that enabled internal etching as the acid has a pathway into the normally isolated grain interior. These tracks show the full length of the track as they are not at an angle to the surface. The length of these tracks is measured, along with the angle of the track relative to the C-axis of the grain using inbuilt software on the BX51 microscope setup. The C-axis orientation is estimated using the track pits, which are longer in the direction of the C-axis. The length of the pits is also measured to gather information on the chemical composition of the grains.

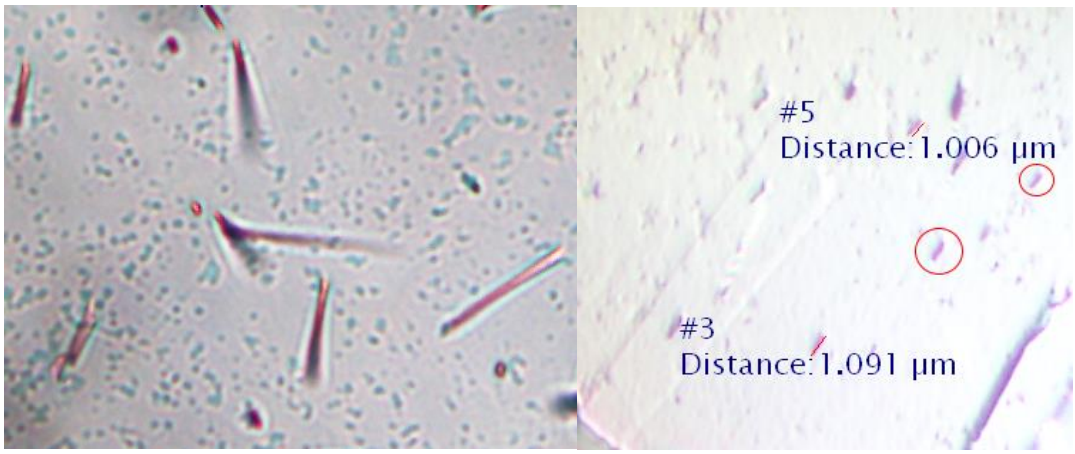

Figure 2. On the left: examples of typical fission tracks under 1000X magnification using transmitted light

On the right: two measured fission track pits and two circled etch pits under 1000X magnification using reflected light

Laser Ablation Inductively Coupled Plasma Mass Spectrometry (LA-ICP-MS)

In order to obtain the apatite fission track age for each analysed apatite grain, both the spontaneous fission track densities (counting results) and an accurate determination of the U concentration are required. An Argilent 7700s quadrupole mass-spectometer coupled to a Resonetics M-50 laser ablation system at Adelaide Microscopy was used to analyse the uranium concentration of the counted apatite grains. Sample slides were cut with a tungsten carbide glass cutting tool in order to fit four rather than two samples into the sample holder. NIST 610, 612 and 614 standards as well as a Durango apatite standard were inserted into the sample holder with the samples for analysis (Fig. 3). After initial plasma ignition and stabilising, the sample holder was inserted into the laser ablation chamber and care was taken that the door was gently and slowly screwed shut to prevent a rush of air blowing the plasma out. Once the laser technician ensured that the oxide levels in the chamber have stabilised and has carried out calibration, analysis could start. A scanned image of the sample holder was mapped to the analytical area to enable navigation to the counted apatite targets. 15 seconds of background was recorded before laser ablation occurred for 30 seconds, after which 15 seconds of cooldown occurred. Then the laser moved a large distance (e.g. between standards and unknowns) an additional 60 seconds of background was allowed in order to allow the gas to settle in the chamber to provide more reproducible results. Repeated measurement of standards was carried out throughout the ablation sequence, using a pattern of two of each of the four standards and eight unknowns repeated ten times. For each analysis, both ^{238}U and ^{235}U isotopes were measured as well as ^{44}Ca as an internal standard.

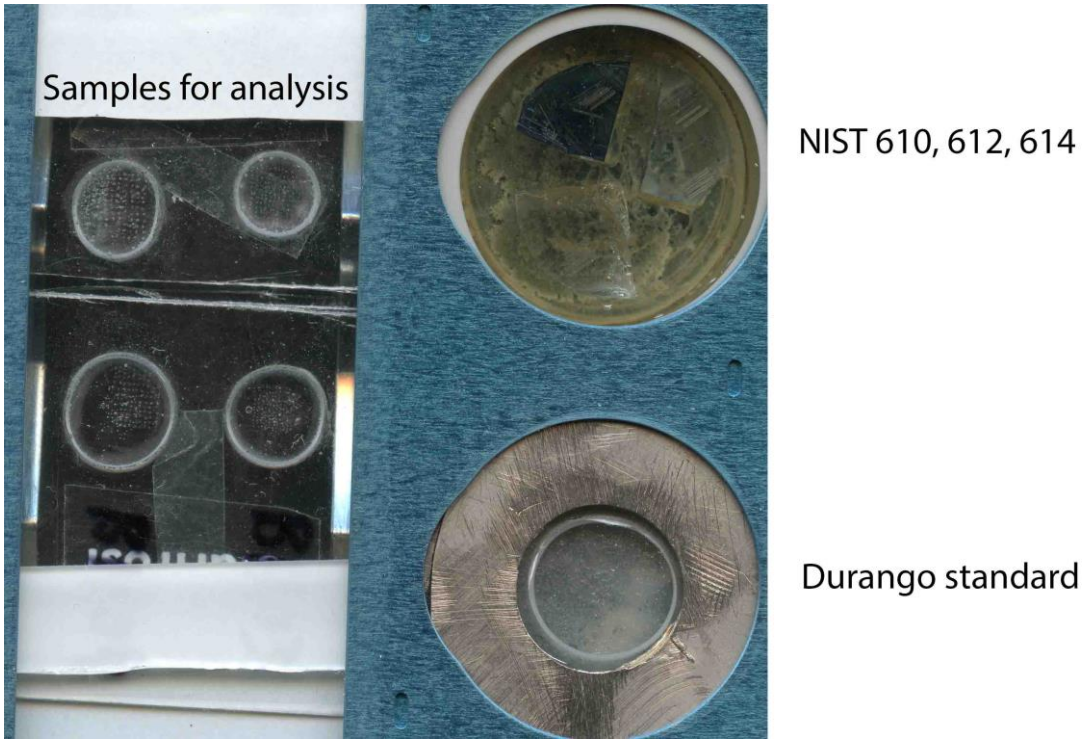

Figure 3. Configuration of the sample holder for the Resonetics M-50 laser ablation system

Data reduction

Data reduction was performed by a series of custom spreadsheets into which the raw data was fed. Each analytical run is examined as a line graph of the U/Ca ratio to check for anomalous features, such as spikes or increasing and decreasing trends. Ideally the graph should be flat, indicating that the ratio is constant and the grain has no detectable zonation or inclusions. If these anomalous features do exist then they are deleted from the data if possible, or if they are too major to be deleted the analytical spot is disregarded and not used. Satisfactory elemental data is then inserted into another spreadsheet where the U-concentrations were calculated using a NIST-calibration line. In the same spreadsheet, cooling ages were then calculated using the age equation below. The Durango standard is used to check the accuracy of the measurements. A combination of all the Durango standard ages is used to calculate a 'zeta' calibration factor. This calibration factor allows the correction of the unknown sample ages not

only against the primary suite of NIST standards, but also against the certified value for the Durango secondary standard. This `double-calibration` approach allows more robust and repeatable determinations of the fission track ages for the individual analysed apatite grains.

Age equation (Hasebe et al., 2004)

$$t=\frac{1}{\lambda_D}\ln\left(1+\frac{\lambda_D \rho_s M}{\lambda_f N_A^{238}\mathrm{U}10^{-6} d R_{sp} k}\right)$$

where λ_D = ^{238}U total decay constant (1.55125×10^{-10} a^{-1}), λ_f = ^{238}U spontaneous fission-decay constant (8.46×10^{-17} a^{-1}), N_A = Avogadro's number (6.02214×10^{23} mol^{-1}), d=apatite density (3.19 g/cm^2 as in Hasebe et al., 2004), M= the atomic mass of ^{238}U (238.0508amu), k = observational parameter = 1 are constants. ^{238}U is the measured 238-Uranium concentration (in μg/g)in the sample, ρ_s is the spontaneous fission track density (in tracks/cm^2) and R_{sp} is a registration factor, and corresponds to the range or to half of the measured mean confined fission-track length.

Electron Probe Micro-analyser (EMPA)

Additional EPMA analyses were carried out to constrain the Cl/F ratio for each counted apatite grain. These data allow the subdivision of apatite grains with different annealing kinetics and annealing resistivities which aids the discrimination of potential multiple age-peaks within each sample. Samples were coated in graphite and placed into the analysis chamber of the JEOL JXA 8100 EPMA by technicians at IGGCAS. Using the analysis software grains that had undergone prior AFT analysis were selected and manually focussed on using a joystick style controller. Data was provided in an excel spreadsheet giving mass percentage values for the elements in the grain.

Modelling

Zeta ages from data reduction are fed, along with the additional Cl/F data, into the RadialPlotter software (Vermeesch 2009) that uses a radial plot to calculate the central age for the single-grain ages for each of the samples. This central age is reported in the data table in the results section and gives the best estimation for the apparent AFT cooling age of the analysed sample. However, multiple AFT age-populations may be present as explained above and the radial plot is further used as a tool to distinguish those. These age-peaks are ideally found by using the automatic mixture model in the software, which uses the uncertainty of the ages to decide if several statistically different populations exist. Different Cl/F ratios and thus different annealing kinetics are colour coded on the radial plots.

HeFTy modelling software was used to model the cooling path (t-T evolution) using the aparant apatite fission track ages and confined length data. High and low temperature constraints were added into the moddeling space to allow the model to run. Other geological constraints (e.g. Ar-Ar cooling ages) were inserted as well if available and possible cooling paths through these constraints were simulated using a Monte-Carlo approach. If a generated cooling path matches the inserted AFT data with a goodness of fit >0.05 the path was retained as a green `statistically acceptable` path. If the cooling path matches the inserted AFT data with a goodness of fit >0.5, it is retained as a purple `good fit path`. After the modelling was terminated using a user-inserted threshold (typically when >100 good paths were obtained), good fit-envelopes were displayed which visualise the thermal history of the investigated sample between ~120C and ambient temperatures.

(U-Th-Sm)/He

In order to refine the thermal history models in the lower temperature range (~80-40C), apatite (U-Th-Sm)/He analysis was performed at on three samples at The John De Laeter Centre for Isoptic Research at Curtin University. 10-15 high quality euhedral, inclusion-free, unbroken apatite crystals with grain size larger than 70µm per sample were selected. These grains were selected in the same way as the grains for AFT analysis except they were placed into a small vial rather than onto a slide. From these separates, the 3 best crystals were selected by Curtin University technical staff and individually loaded into Pt-tubes. These aliquots were individually degassed and measured for their 4He concentration using a Pfeiffer Prisma QMS-200 mass spectrometer. U, Th and Sm concentration measurements were carried out on the Agilent 7500 ICP-MS. Data reduction and age calculation was done using the method described in Evans *et al.* (2004). Where satisfactory AHe data could be obtained, those data was inserted into the thermal history modelling software as well.